Path integral Monte Carlo study of superfluid 4He in disordered narrow nanopores

Vrcan, Hrvoje

Master's thesis / Diplomski rad

2017

Degree Grantor / Ustanova koja je dodijelila akademski / stručni stupanj: **University of Split, University of Split, Faculty of science / Sveučilište u Splitu, Prirodoslovno-matematički fakultet**

Permanent link / Trajna poveznica: https://urn.nsk.hr/urn:nbn:hr:166:921286

Rights / Prava: Attribution-NonCommercial-NoDerivatives 4.0 International/Imenovanje-Nekomercijalno-Bez prerada 4.0 međunarodna

Download date / Datum preuzimanja: **2024-11-27**

Repository / Repozitorij:

Repository of Faculty of Science

UNIVERSITY OF SPLIT

FACULTY OF SCIENCE

SPLIT, JULY 2017

Path integral Monte Carlo study of superfluid ^{4}He in disordered narrow nanopores

DIPLOMA THESIS

AUTHOR

HRVOJE VRCAN

LEANDRA VRANJEŠ MARKIĆ

MENTOR

Basic documentation card

Path integral Monte Carlo study of superfluid ^{4}He in disordered narrow nanopores

Hrvoje Vrcan

ABSTRACT

We present a research of low-energy ^{4}He system confined in a nanopore. The system is studied with Monte Carlo simulations in path integral formulation of quantum mechanics (PIMC simulations), and the underlying theory is provided. Nanopores are set to a narrow radius $R = 3\,\text{Å}$, with the addition of disorder in the form of fictitious atoms scattered randomly around the surface. This system is expected to scale as a Luttinger liquid - a low-energy effective model of one-dimensional systems, which was confirmed for helium in nanopores without disorder. In this work we particularly study the predicted scaling of superfluid fraction with the temperature and length of the nanopore. The superfluid fraction is calculated using PIMC simulations. The obtained data do not fit the theoretical predictions well, that is large χ^2 values are obtained. We discuss the disagreement of the results with the theory of 1D systems.

Istraživanje suprafluidnog ^{4}He u uskim nanoporama s neredom metodom Monte Carlo integrala po stazama

Hrvoje Vrcan

SAŽETAK

Predstavljamo istraživanje ^{4}He adsorbiranog u nanopori na niskim energijama. Sustav je proučavan metodom Monte Carlo simulacija u formalizmu kvantne mehanike integrala po stazama (PIMC simulacije), čija je osnovna teorija objašnjena u radu. Odabran je model uskih nanopora, radijusa $R = 3$ Å, s dodatkom nereda u obliku fiktivnih atoma raspoređenih nasumično blizu površine. Od ovakvog sustava se očekuje skaliranje kao kod Luttingerove tekućine - niskoenergijskog modela jednodimenzionalih sustava, što je potvrđeno za helij u nanoporama bez nereda. U ovom radu posebno proučavamo skaliranje udjela suprafluida s temperaturom i duljinom nanopore. Udio suprafluida izračunali smo korištenjem PIMC simulacija. Dobiveni podaci ne slažu se dobro s teorijskim predviđanjima, odnosno dobivene su velike vrijednosti χ^2-a. Diskutiramo neslaganje rezultata s teorijom 1D sustava.

Contents

1 Introduction

Helium has been a bountiful model element for an abundance of scientific studies for a long time now, mainly because of its unique phase diagram, the only one among elements with liquid phase in the limit of absolute zero. Natural helium comes in two isotopes, bosonic ^{4}He and fermionic ^{3}He. Among the many areas of study of low-energy and ultra-cold physics regarding helium, the phenomena that stand out the most are condensation and superfluidity. Both are purely quantum - impossible for classical systems.

Condensation is an occurrence where the macroscopic part of the system falls into a single state, below some temperature. Obviously, it is only possible for bosonic systems, since the Pauli exclusion principle prevents any two fermions from being in one same state. A condensed system is called Bose-Einstein condensation (BEC), in honor of Albert Einstein and Satyendra Nath Bose, two physicists who predicted this phenomenon in 1924. In an attempt to explain superfluidity, the ability of quantum systems to flow without friction, London used the concept of BEC. The experimental observation of superfluid transition temperature $T_\lambda = 2.17\,\mathrm{K}$ gave rise to the two fluid model for ^{4}He, with a fraction of the system behaving completely without friction, while the rest behaves as a normal liquid. London proposed that the superfluid fraction is actually condensed in the lowest single-particle state. Contrary to that, Landau explained superfluidity as a combination of liquid in ground state as superfluid component, and fluid of quasiparticles as normal component, with no mention of BEC.

London vs. Landau controversy is very much alive, even nowadays. It is still debatable if the occurrence of condensation and superfluidity are connected on a level deeper than coincidental. Still, many modern studies seem to be more inclined towards Landau, viewing the two simply as separate quantum phenomena, and therefore studying one regardless of the other. From a very large number of studies conducted in this niche of physics ever since, one can highlight D. M. Ceperley in 1995 [1], who rounded up R. Feynman's formulation of quantum mechanics from 1948 [2], into a powerful technique for computer simulations.

The focus of this work is the study of superfluidity of bosonic ^{4}He in porous media. A study has been conducted by L. Vranješ Markić and H. Glyde [3], presenting path integral Monte Carlo simulations of various properties of liquid ^{4}He in nanopores. One focal point of the study was the fact that helium seems to scale as a system of different dimensionality, depending on radius of the pores. Specifically, for a very narrow nanopore, it scales as a one-dimensional (1D) liquid. The interesting part is the theory describing a low-energy one-dimensional quantum system - Tomonaga-Luttinger liquid. This effective theory is valid for virtually any one-dimensional system, which makes studying that model applicable to many others. In 1D, long range order is not possible. Instead, 1D Luttinger liquid exhibits long range correlations decaying by power law, even in the limit

of absolute zero. So, the correct terminology in 1D is *quasi-solid*, *quasi-condensate* and *quasi-superfluid*.

The aforementioned study consisted of simulations of low temperature helium liquid confined inside a cylinder whose order of magnitude is in angstroms. This work continues the in-silico study of ^{4}He in very narrow nanopores, but with an addition of disorder, in the form of foreign fixed particles in the outer layers of the cylinder. The disorder will affect the potential that atoms of helium feel. The goal is to observe if the addition of disorder confirms or breaks the Tomonaga-Luttinger model and possibly provide an explanation why, with the target property of interest being the superfluid density.

In 1D there is a prediction that, depending on the so-called Luttinger parameter K, which is connected to the density of the system, different physical regimes are observed. For $K < 1/2$ the system is in the quasi-solid regime. Otherwise it is in superfluid (or more precisely in quasi-superfluid) regime. Furthermore, it has been predicted that for $K > 3/2$, the superfluid is robust to disorder, while for lower K the superfluidity should be destroyed [4]. The aim of this work is also to observe in the *quasi*-1D geometry the change in the superfluid response with the density and specifically to observe if and how one can differentiate these different regimes.

The second chapter of this thesis will present two theories relevant for this study - path integral formulation of quantum mechanics and the Tomonaga-Luttinger model. The third chapter will review Monte Carlo methods of computation, their implementation with the path integral theory, and the way relevant observables are calculated. The fourth chapter will explain in detail the setting of the system, present already known results and the new results, comparing them with the predictions of Luttinger liquid model. Finally, the results will be discussed in the fifth chapter.

2 Theory

In this chapter we will review important theoretical concepts behind the calculations of low temperature helium many-body systems. Since the computational process itself involves the use of path integral Monte Carlo (PIMC) method, it is relevant to understand the basis of Feynman's Path Integral formulation of quantum mechanics. Secondly, according to the calculated properties, the system of low density bosonic helium in a narrow nanopore seems to behave as a Luttinger liquid (LL) - an effective model of low energy one-dimensional systems. The underlying theory for such a system will be described as well.

2.1 Path integral quantum mechanics

The theory of quantum mechanics began with two mathematically equivalent, but yet different formulations - one by Schrödinger, which involves the mechanics of a wave function governed by his famous equation, and the other by Heisenberg, describing instead the time evolution of operators when acting on a quantum state. In this section, a third formulation will be described - one established by Richard P. Feynman in 1948. The theory is centered around finding a complex function whose square is the probability amplitude of finding the system in some region, for minimal classical action of the system [2]. This approach is equivalent to the principle of least action of Hamilton's classical mechanics, passed onto the quantum framework of mind. Aside from providing a different insight into the fuzzy world of quantum systems, this path integral formulation (PI) is fundamental in development of the PIMC method of stochastic computation, which provides some benefits (and some weaknesses) to previously devised methods.

2.1.1 Path integral formalism

Suppose we have a particle that can have various values of a coordinate x. We can make a certain (large) number of successive measurements of its coordinate, each separated by some (small) time interval ϵ. In a classical sense, the successive values of the coordinate define a path $x(t)$. The probability of measuring such a path is a function of successive measurements $P(x_1, x_2, ..., x_i, ...)$. If one wants to know the probability of finding the particle in some space-time region R specified by different intervals of the coordinate x at different times of measurement, $R = \{x_1 \in [a_1, b_1], x_2 \in [a_2, b_2], ...\}$, one should integrate the probability function over all possible values of $\{x_i\}$:

$$P_R = \int_R P(x_1, x_2, ..., x_i, ...) \mathrm{d}x_1 \mathrm{d}x_2 ... \mathrm{d}x_i ... \tag{2.1}$$

From classical perspective, this is completely correct because it is possible to measure the system at any time without disturbing it.

In the quantum world, however, this is only true if such detailed series of measurements were actually made and only the paths lying in R were taken into consideration. To avoid ambiguous uncertainties, an *ideal measurement* should be made - one that only determines if the system is in region R, without disturbing it further. It is expected that the probability that the particle is found in R is the square of some complex number $|\varphi(R)|^2$ whose phase corresponds to the probability density function P found in Eq. 2.1.

To provide mathematical framework and allow computation of quantities, Feynman formulated his theory with two postulates [2]:

1. If an ideal measurement is performed to determine whether a particle has a path lying in a region of space-time, then the probability that the result will be affirmative is the absolute square of a sum of complex contributions, one from each path in the region.

2. The paths contribute equally in magnitude, but the phase of their contribution is the classical action (in units of $\hbar$); i.e. the time integral of Lagrangian taken along the path.

To be able to calculate the action $S = \int L(\dot{x}, x)\mathrm{d}t$, it is necessary to have a path $x(t)$ as a continuous function of time, so the $\epsilon \to 0$ limit is expected to be taken at some point. The action can be expressed as

$$S = \sum_i S(x_{i+1}, x_i), \tag{2.2}$$

with

$$S(x_{i+1}, x_i) = \min \int_{t_i}^{t_{i+1}} L\left(\dot{x}(t), x(t)\right) \mathrm{d}t. \tag{2.3}$$

Lagrangian must not depend on any higher time derivatives of the position than the first, or the end points are not sufficient to define a classical path $x(t)$ which minimizes the action. This means that the contribution of the path $x(t)$ to the function from the first postulate must be proportional to $\exp\left[\frac{i}{\hbar} S\left(x(t)\right)\right]$. Additionally, the sum in Eq. 2.2 is infinite for infinite time intervals, so the theory has to be limited to finite time [2].

Combining Eq. 2.2 with the postulates, one can construct a function

$$\varphi(R) = \lim_{\epsilon \to 0} \int_R \exp\left[\frac{i}{\hbar} \sum_i S(x_{i+1}, x_i)\right] \dots \frac{\mathrm{d}x_{i+1}}{A} \frac{\mathrm{d}x_i}{A} \dots, \tag{2.4}$$

where $\frac{1}{A}$ is the normalization factor for each time (whose value is not specified). Now the complex valued function whose square is the probability amplitude to find the system in a certain region of space-time has been defined. This completes the path integral formulation of quantum mechanics.

It is possible to show the analogy between this function and the wave function in the standard formulation of quantum mechanics. A certain part of the region R can be

specified as a reference to define the past and the future, i.e. the given state of the system and the experiment of measurement performed on the system, respectively. This part can, time-wise, be as narrow as wanted. Suppose that a certain index k of consecutive measurements x_i denotes that part. Then, every measurement before, x_{k-1}, x_{k-2}, ... marks the past, and every one after x_{k+1}, x_{k+1}, ... the future. This splits the region R into two parts: R' for the past, and R'' for the future. To get φ, Eq. 2.4 is applied on both of the intervals, and then integral is taken over the one remaining measurement x_k. The index can be omitted here so the measurement is simply called x.

$$\varphi(R) = \int \chi^*(x,t)\psi(x,t)\mathrm{d}x. \tag{2.5}$$

Here, ψ stands for the function from Eq. 2.4 integrated over the past R', and χ^* the same function[1] integrated over the future R''. Since x appears as the $k-th$ index of the action sum exponent in both integrals, it is the only measurement on which both functions depend after the integration. Now it is valid to say that $|\varphi(R)|^2 = \left|\int \chi^*(x,t)\psi(x,t)dx\right|^2$ is the probability that the system initially in state ψ will be found in state χ by experiment. Then, both of these functions can be considered wave functions, one for the state before the experiment, and one after. Also, if two systems are prepared in a different way, meaning they come from different past space-time regions, but yield the same ψ, then the future measurements cannot distinguish the region from which the system came. Likewise, if two systems yield the same χ for different measurement experiments, then those experiments are equivalent [2].

Feynman showed that the wave function defined this way satisfies the Schrödinger equation under certain conditions. According to Eq. 2.4, computing the function ψ in the next instant of time, after one small time interval ϵ, would result in

$$\psi(x_{k+1},t) = \int \exp\left[\frac{i}{\hbar}S(x_{k+1},x_k)\right]\psi(x_k,t)\frac{\mathrm{d}x_k}{A}. \tag{2.6}$$

The equivalence between Eq. 2.6 and the wave equation is only true in the limit $\epsilon \to 0$. The expansion of this equation in the first order of ϵ is considered to be valid for very small time intervals. Also, this illustration will be done for particle in one spatial dimension in a potential $V(x)$. This way, it is possible to approximate the action with a very simple expression:

$$S(x_{i+1},x_i) = \frac{m\epsilon}{2}\left(\frac{x_{i+1}-x_i}{\epsilon}\right)^2 - \epsilon V(x_{i+1}). \tag{2.7}$$

This case can easily be generalized to more dimensions and coordinates other than Cartesian. With some algebra and after integration, Eq. 2.6 becomes

$$\psi(x,t+\epsilon) = \exp\left(\frac{-i\epsilon V(x)}{\hbar}\right)\frac{\sqrt{\frac{2\pi\hbar\epsilon i}{m}}}{A}\left[\psi(x,t) + \frac{\hbar\epsilon i}{2m}\frac{\partial^2 \psi}{\partial x^2} + ...\right]. \tag{2.8}$$

---

[1]The asterisk marks complex conjugation. It is more convenient to define this function as a complex conjugate of some function χ.

This can be expanded in the first order of ϵ, with the left-hand side changing to $\psi\left(x, t+\epsilon\right) = \psi\left(x, t\right) + \epsilon \frac{\partial \psi(x,t)}{\partial t}$ and the exponent containing potential to $\exp\left(\frac{-i\epsilon V(x)}{\hbar}\right) = 1 - \frac{i\epsilon V(x)}{\hbar}$. Also, to keep both sides of the equation in the same order of ϵ, it is necessary that $A = \sqrt{\frac{2\pi\hbar\epsilon i}{m}}$. Then, the equation changes to

$$-\frac{\hbar}{i}\frac{\partial \psi}{\partial t} = \frac{1}{2m}\left(\frac{\hbar}{i}\right)^2 \frac{\partial^2}{\partial x^2}\psi + V(x)\psi, \qquad (2.9)$$

which is exactly the Schrödinger equation in one dimension [2]. It may be worthwhile to mention that this demonstration was carried out for the case of Lagrangian being the quadratic function of velocities, which enables the easier calculation of the integrals over classical path taken by a free particle.

The equation 2.6, which describes the evolution of a wave function in a small time interval, is the physical expression of the Huygens' principle, for quantum objects. The principle states that, if one knows the amplitude of a wave on a certain surface, the amplitude in a nearby point is a sum of contributions from all the points on the surface. The contributions are delayed in phase according to the time it would take to get from the point on the surface to the given point along the path of the least time. In a similar fashion, one can consider the amplitude of the wave function ψ at some time $t + \epsilon$ as the sum of all contributions of the wave function from a "surface" of points x in some previous moment t. The contributions are delayed in phase by the amount of action required to move from the surface to the given point along the path of the least action, which is the classical action in Eq. 2.7 [2].

It is clear that, in this comparison, time is replaced by action and plays a similar role. This concludes the analogy between the wave function in standard and PI formulations of quantum mechanics.

2.1.2 Imaginary time path integrals

Suppose we have a system prepared in an initial state ψ at some time t_0 and we want to calculate the probability that the system will be found in a later state χ at a time t_j. The result will be the square of the transition amplitude

$$\left\langle \chi_{t_j} \mid \psi_{t_0} \right\rangle = \lim_{\epsilon \to 0} \int ... \int \chi^*\left(x, t\right) \times \exp\left(\frac{i}{\hbar}S\right)\psi(x,t)\frac{\mathrm{d}x_0}{A}...\frac{\mathrm{d}x_j}{A}. \qquad (2.10)$$

From the perspective of interaction picture representation of standard quantum mechanics, this is nothing but a matrix element of $\exp\left(-\frac{i(t_j - t_0)\hat{H}}{\hbar}\right)$ between states ψ_{t_0} and χ_{t_j}. Matrix elements of any function of the coordinates F can be calculated by simply adding it into the product of states:

$$\left\langle \chi_{t_j} \mid F \mid \psi_{t_0} \right\rangle = \lim_{\epsilon \to 0} \int ... \int \chi^*\left(x, t\right) F(x_0, ..., x_j) \times \exp\left(\frac{i}{\hbar}S\right)\psi(x,t)\frac{\mathrm{d}x_0}{A}...\frac{\mathrm{d}x_j}{A}. \qquad (2.11)$$

In the $\epsilon \to 0$ limit, F becomes a functional of the path $x(t)$. Similarly to the standard formulation condition that we can measure only Hermitian operators, or observables,

here we establish a condition that we can measure only those functionals that can be defined by the changes produced by the possible changes in action S. Such quantities are denoted as *observable functionals* [2]. This class of functionals is restricted by the restrictions on action originating from the condition that the Lagrangian be a quadratic function of velocities.

Following a similar approach as presented so far, it is possible to determine how to measure quantities of a quantum statistical system. For a quantum system in thermal equilibrium, all the properties can be calculated from the thermal density matrix [1, 5]. For Hamiltonian $\widehat{H}$ and at temperature T, the thermal density matrix is

$$\widehat{\rho} = \frac{1}{Z} e^{-\beta \widehat{H}} = \frac{1}{Z} \sum_i e^{-\beta E_i} |\psi_i\rangle \langle \psi_i| . \tag{2.12}$$

Here, $\beta = \frac{1}{k_B T}$, where k_B is the Boltzmann constant, ψ_i are eigenfunctions of Hamiltonian $\widehat{H}$ with eigenvalues E_i, and Z is the partition function

$$Z = \text{Tr}(e^{-\beta \widehat{H}}) = \sum_i e^{-\beta E_i}. \tag{2.13}$$

Any observable $\widehat{O}$ can be calculated via density matrix as

$$\widehat{O} = \text{Tr}\left(\widehat{O}\widehat{\rho}\right) = \frac{1}{Z} \sum_i e^{-\beta E_i} \langle \psi_i | \widehat{O} | \psi_i \rangle . \tag{2.14}$$

In the coordinate representation, all elements of the thermal density matrix are non-negative and thus can represent probability. We will denote with $\mathbf{R}_m = \{\mathbf{r}_{1,m}, ..., \mathbf{r}_{N,m}\}$ a set of coordinates $\mathbf{r}_{j,m}$, or a configuration, of N particles, with m being the index of the configuration and j of an individual particle [5]. In the position space, density matrix is a function of two configurations $\mathbf{R}_1$ and $\mathbf{R}_2$, so $6N$ variables, with a parameter β [1]:

$$\widehat{\rho}(\mathbf{R}_1, \mathbf{R}_2; \beta) = \langle \mathbf{R}_1 | e^{-\beta \widehat{H}} | \mathbf{R}_2 \rangle = \frac{1}{Z} \sum_i \psi_i^*(\mathbf{R}_1) e^{-\beta E_i} \psi_i(\mathbf{R}_2). \tag{2.15}$$

The expectation value of any observable operator $\widehat{O}$ can be calculated as

$$\langle \widehat{O} \rangle = \int d\mathbf{R}_1 d\mathbf{R}_2 \, \widehat{\rho}(\mathbf{R}_1, \mathbf{R}_2; \beta) \, \langle \mathbf{R}_1 | \widehat{O} | \mathbf{R}_2 \rangle . \tag{2.16}$$

The property of the density matrix crucial for the development of PIMC method is the convolution of exponential operators [1]

$$e^{-(\beta_1 + \beta_2)\widehat{H}} = e^{-\beta_1 \widehat{H} - \beta_2 \widehat{H}}. \tag{2.17}$$

This means that the product of two density matrices is also a density matrix, with a different parameter equal to the sum of component parameters. In the position representation, this convolution is written as

$$\widehat{\rho}(\mathbf{R}_1, \mathbf{R}_3; \beta_1 + \beta_2) = \int d\mathbf{R}_2 \, \widehat{\rho}(\mathbf{R}_1, \mathbf{R}_2; \beta_1) \, \widehat{\rho}(\mathbf{R}_2, \mathbf{R}_3; \beta_2). \tag{2.18}$$

It is simple to extend this to the product of more than two density matrices. The parameter β can be separated into M equal parameters $\epsilon = \frac{\beta}{M}$, and thus the density matrix into a product of M density matrices, each with the parameter ϵ. Then the convolution of operators in Eq. 2.17 becomes

$$e^{-\beta \widehat{H}} = \left(e^{-\epsilon \widehat{H}} \right)^M, \tag{2.19}$$

and the convolution of density matrices in Eq. 2.18 changes to [1, 5]

$$\widehat{\rho}(\mathbf{R}_1, \mathbf{R}_{M+1}; \beta) = \int d\mathbf{R}_2 d\mathbf{R}_3...d\mathbf{R}_M \, \widehat{\rho}(\mathbf{R}_1, \mathbf{R}_2; \epsilon) \, \widehat{\rho}(\mathbf{R}_2, \mathbf{R}_3; \epsilon)... \, \widehat{\rho}(\mathbf{R}_M, \mathbf{R}_{M+1}; \epsilon) \tag{2.20}$$

This formula is central to the Monte Carlo implementation of the Path Integral formalism. Consider that the form of Eq. 2.12 defines the density matrix as an evolution operator in imaginary time $t = i\beta$. Then Eq. 2.20 describes the evolution in imaginary time of an initial configuration $\mathbf{R}_1$ to the final configuration $\mathbf{R}_{M+1}$, written through M intermediate steps, each with an individual configuration $\mathbf{R}_i$. This sequence of configurations $\mathbf{R}_1, \mathbf{R}_2, ..., \mathbf{R}_{M+1}$ can be interpreted as path in imaginary time. Additionally, since the imaginary time parameter β is closely tied to temperature, so are the smaller parameters ϵ. In fact, the intermediate steps represent a division of the time evolution into evolutions with a smaller time interval $t' = i\epsilon = \frac{t}{M}$. This means that the temperature of the system for each smaller time evolution is MT. Loosely speaking, this can be interpreted as measuring the system M consecutive times on M times the higher temperature. Even for finite $M \geq 1$, the Eq. 2.20 is exact. Of course, one can make the $M \to \infty$, or $\epsilon \to 0$ limit to make the path continuous [5]. This makes the temperature infinite and measurements completely classical.

The action of a system is minus the natural logarithm of the density matrix

$$S = -\ln [Z\widehat{\rho}]. \tag{2.21}$$

Just like in Eq. 2.2, or considering the density matrix convolution Eq. 2.18, we can separate the action into smaller pieces [5]

$$S_m = -\ln [\widehat{\rho}(\mathbf{R}_{m-1}, \mathbf{R}_m; \epsilon)]. \tag{2.22}$$

This way, the exact thermal density matrix from Eq. 2.20 becomes [1]

$$\widehat{\rho}(\mathbf{R}_1, \mathbf{R}_{M+1}; \beta) = \int d\mathbf{R}_2 d\mathbf{R}_3...d\mathbf{R}_M \times \exp \left[\sum_{m=2}^{M+1} S_m \right]. \tag{2.23}$$

Since the exact thermal density matrix is calculated from the Hamiltonian $\widehat{H} = \widehat{K} + \widehat{V}$, Eq. 2.22 suggests that the action will also have kinetic and potential parts. The exact *kinetic action* K_m between $(m-1)$-th and m-th time interval is

$$K_m = \frac{3N}{2} \ln(4\pi\lambda\epsilon) + \frac{(R_{m-1} - R_m)^2}{4\lambda\epsilon}, \tag{2.24}$$

where $\lambda = \frac{\hbar^2}{2m}$. The potential part of the action U_m, or the *inter-action* [1], is what remains:

$$U_m = S_m - K_m. \tag{2.25}$$

To calculate the matrix elements of observables, a sufficient approximation is required for action, and therefore the density matrix. This will be reviewed in the next chapter.

2.1.3 The classical isomorphism

Path integral formulation of a thermal quantum system allows making of an important interpretation that may shed some light on what we can expect from its properties.

Firstly, notice that by dividing the imaginary time into M smaller time intervals ϵ, the system of N particles is actually represented by M different configurations. One configuration, represented by the set of coordinates $\mathbf{R}_m$, is called a *time slice* or *time sweep*. Following the logic of depicting imaginary time as the actual, real time, each configuration will be connected only to the previous and the next one, which expresses the physical causality. This connection is defined by the action Eq. 2.22 and is called a *link* [1, 5].

Although it may be tempting to see imaginary time as just a different way of introducing time, it's actually not a time at all, in a physical sense. In fact, imaginary time is by all accounts another spatial dimension in physical systems. However, being that one cannot just introduce a new spatial dimension to a quantum system, this has a distinct interpretation, that is, a connection to the classical systems. Every d-dimensional quantum system in imaginary time can be mapped onto a classical system of $d + 1$ dimensions, where the quantum imaginary time direction plays the role of an additional classical spatial dimension [6]. So, a quantum system of N particles with M different configurations is analogous to a classical system of $N \times M$ particles. Each particle here is called a *bead* [5] and specified by the coordinate $\mathbf{r}_{j,m}$ of each configuration $\mathbf{R}_m$.

Each particle can interact only with other particles in the same configuration. However, each particle is also propagated in imaginary time, so it is connected to the previous and next versions of itself, forming a path in imaginary time. The kinetic action connects a bead with other beads of the same index j and in different configurations m. This just means that the kinetic energy propagates the particles in time. The potential action connects the beads with different j in the same configurations m, which accounts for physical interactions dependent on the coordinates of particles. In a classical analogy, this means that the kinetic action of the form Eq. 2.24 connects the beads with a quadratic spring potential, so the particles form chains in what would be the imaginary time. These chains are called *polymers* [1, 5]. The interpolymeric potential is peculiar in a classical sense, since it only interacts in the same link, or at the same time in a quantum sense.

Furthermore, convolution property of the density matrix produces a periodic boundary condition $R_1 = R_{M+1}$ as a necessary demand for calculation of diagonal observable averages. This means that the polymers in the classical system are closed rings. All this is schematically shown in Fig. 2.1. In a classical system, the action from Eq. 2.21 represents a potential energy function divided by a fictive temperature factor $k_B T$. One
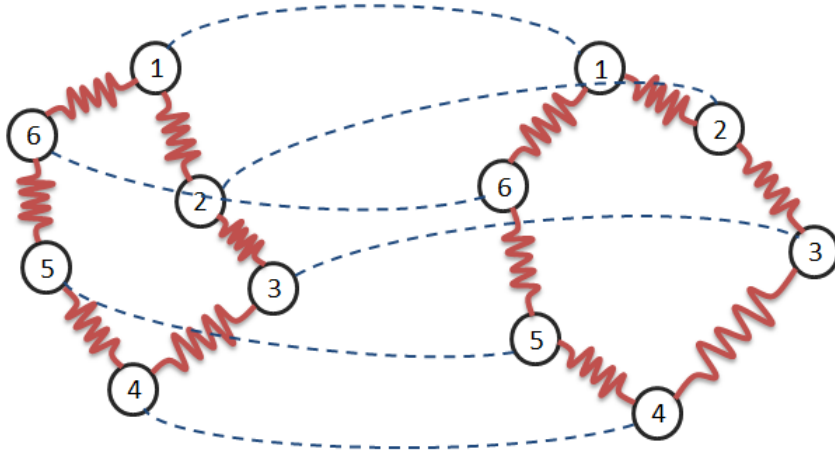
Figure 2.1: A classical isomorphism of a quantum system in an imaginary time. Only two
polymers are shown. The beads with the same number represent particles on
different polymers at the same time. Red springs represent kinetic action
between beads in a single polymer, while blue dashed lines represent the
interpolymeric potential acting in the same time slice. This potential can, of
course, originate from all particles of the same time slice.

polymer corresponds to a path of a particle in imaginary time. Just like real polymers,
these paths are actually fractals by nature [1] - if the number of time slices, and thus the
beads, is infinite, they will not occupy the whole space, but rather a finite region.

This analogy between a quantum system of N particles and a classical system of N ring
polymers with M links is the essence of PI formulation. Partition functions of the two
systems are equal and all of the correlations are calculated the same way. This means
that many properties of the quantum system can be understood in terms of classical
statistical mechanics. Actually, one important remark for this work - superfluidity in the
quantum model, is equal to the presence of macroscopic polymers in the classical model.

There are, however, some conflicts in quantum and classical terminology that may
cause misconceptions, mostly regarding the relation between velocity and temperature.
At low temperatures, system particles are expected to be delocalized - spread out because
of the uncertainty relations. On the other hand, since the velocity is defined as the
displacement of beads between consecutive time slices divided by ϵ, spread out particles
will have higher velocity, which contributes to the higher temperature in a classical sense.
It is important to notice that, for a classical bead-spring model, temperature introduced
in quantum system is not a temperature at all, but just a constant divisor of the potential
energy [5].

2.2 Luttinger liquid model

This section deals with the theoretical model for one-dimensional system of interacting quantum particles. A starting point for the description of these systems is the Fermi gas - a phase of matter comprising large number of non-interacting fermions, particles that obey the Pauli exclusion principle, which prevents them from condensing into a single state like bosons. At absolute zero, the gas is degenerate, meaning that the system's ground state can be obtained by filling all single-particle states up to the Fermi energy [7].

The expansion of this model into the interacting fermions was introduced by Landau in 1956, and is called Fermi liquid [8]. The main idea is to adiabatically introduce the interactions into the non-interacting system, thus transforming its ground state. The adiabatic nature of this transition conserves the quantum numbers of the occupied states, while changing their dynamical properties. This means that there is a one-to-one correspondence between Fermi gas excited states and Fermi liquid states, also called *quasi-particles*. In a physical sense, these quasiparticles can be thought of as propagating fermions that are "dressed" by the interactions, meaning that they are altered by their surroundings to have different effective mass and dynamical properties. Even at $T = 0\,\mathrm{K}$, the Fermi surface of this system is destroyed by the interaction, and in fact has a discontinuity, which makes a big difference in comparison to the Fermi gas [7, 8].

In one dimension, however, the Fermi surface is actually only two points of positive and negative Fermi momentum. The Fermi liquid model breaks down in this case. The simplest model of a system like this describes the low-lying excitations around those two points of a one-dimensional Fermi gas with density-density interactions. This is called the Tomonaga-Luttinger liquid [9].

2.2.1 One-dimensional fermion system

We start by observing the dispersion relation of a one-dimensional system with density-density interactions. Since we are studying the low-lying excitations, most of its physics comes from the vicinity of two Fermi points, which is an equivalent of a Fermi surface in one dimension. Then, the system's dispersion relation can be treated as linear, as shown in Fig. 2.2. This is the Tomonaga-Luttinger model, describing a chiral liquid consisting of two parts, one made up of left moving, and the other of right moving fermions [7, 9].

Second quantization Hamiltonian of this model is

$$\widehat{H} = \sum_{\alpha=\pm 1} v_F \int \mathrm{d}x \psi_\alpha^\dagger (i\alpha\partial_x - k_F)\psi_\alpha - \frac{1}{2} \int \mathrm{d}x\mathrm{d}x' \rho(x)V(x-x')\rho(x'). \qquad (2.26)$$

Here, the index α is $+1$ for right moving subsystem with corresponding field ψ_+, and -1 for left moving subsystem with field ψ_-, v_F is the Fermi velocity, and $\rho = \psi_-^\dagger \psi_- + \psi_+^\dagger \psi_+^\dagger$ is the total density. This microscopic Hamiltonian is exact and is a realistic description of a system with interaction V. However, since we are studying a strongly interacting system with multiparticle excitations, it is very difficult to treat it exactly, so an effective theory is more desirable. Note, however, that Eq. 2.26 makes no distinction between
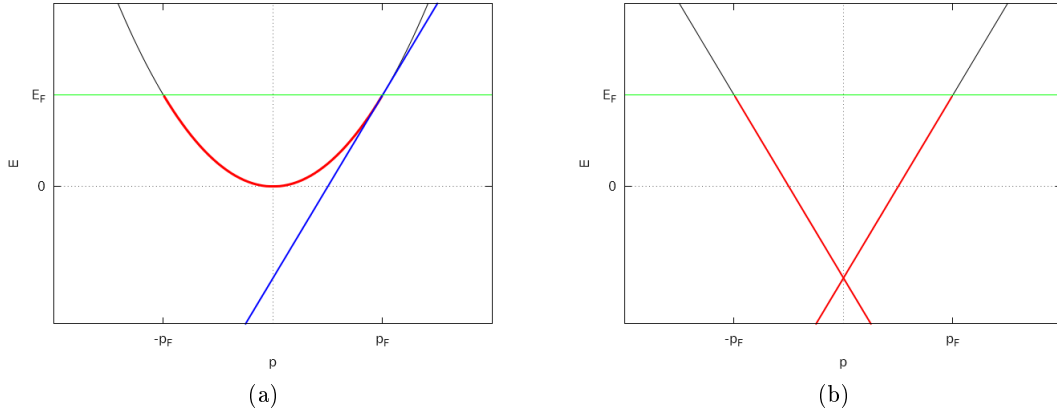
(a)   (b)

Figure 2.2: Dispersion relation of a one-dimensional system. Horizontal green lines de-
note the Fermi energy level, while red lines represent filled states. (a) A more
realistic realization that corresponds to a parabolic band in a one-dimensional
crystal. Blue line is the liearization of the band near the point of positive
Fermi momentum. (b) Dispersion of the Tomonaga-Luttinger model, consist-
ing of right and left moving fermions and an unphysical infinite "sea" of filled
states.

fermions and bosons because, in essence, there is not much difference in 1D [7]. In fact,
using the *bosonization* method, it is possible to express the fermionic fields in terms of
bosonic fields.

Let's begin with one-dimensional bosonic field theory, where the field ϕ is governed by
the non-linear Schrödinger equation (NLSE) for spinless particles of mass m and with
density-density interaction [7]:

$$i\frac{\partial\phi(x,t)}{\partial t} = -\frac{1}{2m}\frac{\partial^2\phi(x,t)}{\partial x^2} + \int \mathrm{d}x'\phi^\dagger(x',t)V(x-x')\phi(x,t), \qquad (2.27)$$

with $\hbar = 1$. The system obeys a periodic boundary condition $\phi(x+L) = \phi(x)$. Since the
physical objects in question are still particles, assume that x is discrete and fields can be
written as $\phi(x_i,t) = \phi_i(t)$. Then the action is

$$S = \int \mathrm{d}t \left[\sum_i \phi_i^\dagger i\partial_t\phi_i - H\right]. \qquad (2.28)$$

This form highly resembles the action of a set of canonical variables, usually written as
$S = \int \mathrm{d}t\,[\mathrm{p}\dot{\mathrm{q}} - H(\mathrm{p},\mathrm{q})]$. The fields ϕ and $\phi^\dagger$ are indeed canonically conjugate variables,
which implies the following commutation relation:

$$\left[\phi_i(t),\phi_j^\dagger(t)\right] = \delta_{ij}. \qquad (2.29)$$

Whichever parametrization we chose for our fields, there must always be a pair of canonical variables with a delta function commutator. There is one such representation for the creation field that can always be used:

$$\phi^\dagger = \sqrt{\rho}e^{i\varphi}, \tag{2.30}$$

where ρ represents the density, and φ represents the phase of the field. For N particles at positions x_n, the density is just a sum of delta functions [7, 8]:

$$\rho(x) \equiv \sum_{n=1}^{N} \delta(x - x_n). \tag{2.31}$$

If the parametrization in Eq. 2.30 is inserted into Eq. 2.29 and the discrete terminology is used, assuming the variables on different sites of the lattice commute, one gets

$$\left[\rho_i, e^{i\varphi_j}\right] = e^{i\varphi_j}\delta_{ij}, \tag{2.32}$$

which immediately leads to

$$[\varphi_i, \rho_j] = i\delta_{ij}. \tag{2.33}$$

It is now clear that the density factor ρ and the phase factor φ can be considered canonically conjugate variables.

The next step is to go back to the continuum description via the mean field approach. Keep in mind that the low momentum, that is long wavelength part of the theory is being studied. For a system of N particles periodic in L, the short distance cutoff is $a = L/N$, and the high momentum cutoff is just the average density $\rho_0 = N/L$. One simple way to set up a continuum approximation for Eq. 2.33 would be

$$\left[\varphi(x), \rho_S(x')\right] = i\delta(x - x'). \tag{2.34}$$

The index "S" stands for smooth or smeared density. However, Eq. 2.34 is not compatible with the general definition of density in Eq. 2.31, so ρ_S cannot be the full density. Still, it is a component of ρ corresponding to the low momentum and long wavelength [7], in accordance with the cutoffs.

It may seem that this crude approximation dismisses the fine particle effects on microscopic scale because of the density smearing. It is possible to reintroduce particle effects, even in the low momentum approximation, by introduction of a new field θ in new parametrization of the density:

$$\rho_S(x) = \rho_0 + \Pi(x) = \frac{1}{\pi}\frac{\partial\theta(x)}{\partial x}. \tag{2.35}$$

Here, a new field Π is also introduced as the shift of ρ_S from the mean density ρ_0, and it it also canonically conjugate to φ. Eq. 2.35 leads to the commutator $[\varphi(x), \theta(x')] = \frac{i\pi}{2}\text{sign}(x-x')$. The new angular field θ is a convenient way to count the particles because it increases by π for every particle, so $\theta(x_n) = n\pi$, where x_n is the coordinate of n-th

particle. With the introduction of new fields in mind, the density can once again be redefined as [7, 8]

$$\rho_G(x) = \frac{1}{\pi} \partial_x \theta(x) \sum_{n=1}^{N} \delta\left(\theta(x) - n\pi\right).$$ (2.36)

This formula is Haldane's ansatz [7, 10] for the granular (index "G") density operator and it is central to this combination of mean field and microscopic approach. The density ρ_G is now actually compatible with the definition in Eq. 2.31. Poisson summation formula can be applied to Eq. 2.36, leading to [8, 10]

$$\rho_G(x) = \frac{1}{\pi} \partial_x \theta(x) \sum_{m=-\infty}^{\infty} e^{i2m\theta(x)}.$$ (2.37)

This form is convenient for approximations since it allows keeping only a certain number of low terms.

At this point, it is possible to reconstruct the actual fields of creation and annihilation $\phi^\dagger$ and ϕ. Although the starting point was a bosonic theory, the whole procedure would have marginal difference for fermions, allowing one to express the local *fermion* fields in terms of low momentum *boson* fields. This essential idea is the reason this method is referred to as *bosonization*. In the virtue of Eq. 2.30 and Eq. 2.37, the bosonic creation operator is defined as

$$\Psi_B^\dagger(x) = A \left\{ \sqrt{\rho_0 + \Pi(x)} \sum_m e^{i2m\theta(x)} \right\} e^{i\varphi(x)}$$ (2.38)

up to an unspecified normalization constant A. The term in $\{...\}$ brackets is the density factor in the form of Eq. 2.37, while the rest is an exponential of the phase factor, just like in Eq. 2.30. The fermion operator is obtained by simply boosting the index of the boson operator by $+1/2$:

$$\Psi_F^\dagger(x) = A \left\{ \sqrt{\rho_0 + \Pi(x)} \sum_m e^{i(2m+1)\theta(x)} \right\} e^{i\varphi(x)},$$ (2.39)

which then satisfies the Fermi statistics [7]. It may be worthwhile to mention the lowest approximations of these two fields:

$$\Psi_B^\dagger(x) \approx \sqrt{\rho_0} e^{i\varphi},$$ (2.40)

$$\Psi_F^\dagger(x) \approx \sqrt{\rho_0} \left(e^{i\theta(x)} - e^{-i\theta(x)} \right) e^{i\varphi}.$$ (2.41)

2.2.2 Properties of a Luttinger liquid

Now that the way to determine the fields has been constructed, the Hamiltonian of this theory can be expressed. In the expansion of energy around constant density and zero

current, dominating terms will be of the second order. So, the most general *effective* Hamiltonian is [10]

$$\widehat{H} = \frac{\hbar}{2\pi} \int \mathrm{d}x \left[v_J (\partial_x \varphi)^2 + v_N (\partial_x \theta - \pi \rho_0)^2 \right], \qquad (2.42)$$

where $\hbar$ was returned for completeness. Two free parameters v_N and v_J are velocities that depend on the interaction and come from the exact microscopic Hamiltonian in Eq. 2.26. In a 1D Galilean invariant system, the parameters are

$$\hbar v_J = \frac{\pi \hbar^2 \rho_0}{m}, \qquad (2.43)$$

$$\hbar v_N = (\pi \rho_0^2 \kappa)^{-1}, \qquad (2.44)$$

where κ is the compressibility. The Hamiltonian is sometimes defined with different parameters [8]:

$$\widehat{H} = \frac{\hbar}{2\pi} \int \mathrm{d}x \left[\frac{v_S K}{\hbar^2} (\partial_x \varphi)^2 + \frac{v_S}{K} (\partial_x \theta - \pi \rho_0)^2 \right], \qquad (2.45)$$

where $K = \sqrt{v_J / v_N}$ is called Luttinger parameter and $v_S = \sqrt{v_J v_N}$ is the speed of sound. Either way, the parameters originate from the fine details of the elusive microscopic Hamiltonian. However, they are independent of the thermodynamical properties such as temperature. This means that, once the parameters of a certain system are set, they are valid for all of its realizations, as long as it is within the theoretical framework of used approximations. They can be calculated for one known realization and reliably used in others.

Basically, a Luttinger liquid spreads any excitation rapidly throughout the entire system. Imagine introducing a localized low-energy excitation, for example acceleration of one particle. This change will spread to the nearest neighbors, who will in turn spread it onto their neighbors, and so on. The difference between this occurrence in one-dimensional and multi-dimensional systems is that in 1D, the excitations are strictly longitudinal; there are no possible transverse components, no dissipation and thus all the excitations are smeared through the system easily. There are no quasiparticles and any disturbance quickly gives rise to a collective excitation [4, 11]. That is why it is necessary to combine the mean field and particle approaches to obtain the coarse-grained approximation in Eq. 2.36.

Still, the derivations and conclusions presented in the previous section are mostly heuristic - to obtain the exact results, one would have to start from the microscopic Hamiltonian in Eq. 2.26 and arrive at the outcome through series of manipulations. Nevertheless, there is a benefit from the heuristic approach. The particles are never actually specified as bosons, fermions, some multiparticle excitations or anything really, so the physics can effectively apply to a wide array of systems. Furthermore, the Luttinger liquid theory is generic and applicable as an effective low-energy theory to virtually *all* one-dimensional systems, making it a de facto fixed point of all such theories [7, 8, 10]. The theory is qualitatively valid even in more realistic cases of non-linear dispersion, as long as it is within the low energy region.

Luttinger liquid theory is dependent on two generally undefined parameters and once they are calculated, all the properties of systems can be obtained exactly. The parameters control all the correlation functions and are thus enough to obtain all the low-energy properties of the model. Specifically, as a very important remark, all asymptotic properties have exponentially decaying dependence on the parameter K. The parameters can be computed analytically using perturbation or numerically if no analytical method is available for a given system. They can be linked with thermodynamic properties, which means they have to be less susceptible to finite-size effects. It is possible to evaluate them based on some general rules. For instance, for fermions, $K > 1$ means attractive interaction, while $K < 1$ means repulsive interactions [8]. Also, as a property of interest for this work, studies show that in disorder, robust superfluidity is possible for $K > 3/2$, while for $K < 3/2$ the system is in Bose glass phase [4].

2.2.3 Superflow

As for the properties of superflow, one must measure the superfluid fraction of a system, that is superfluid density divided by the density of the system. Superfluidity phenomenon is often distinguished as a response to movement of the boundaries enclosing the system. The fraction of the system that does not respond to rotations of the walls is considered to be normal, while the rest is in superfluid phase. In 1D, superfluidity is possible only if state of the system is a superposition of special, topologically coherent states with a slow phase gradient. The reason for this is found in current of particles J through the periodic boundaries of the system. Existence of superfluidity indicates that J is a good quantum number, which is valid only if its eigenstates are orthogonal, meaning their overlap is zero. This is true if they are very different everywhere in available space; that is, if their phase gradient is macroscopically slow [6]. This is in agreement with the description of excitations in LL theory.

In path integral calculations of systems in imaginary time, like the one we are dealing with, it is more convenient to use the current's dual coordinate - winding number W:

$$W = \frac{1}{L} \sum_{n=1}^{N} (x_{\mathcal{P}_n} - x_n), \tag{2.46}$$

where L is the system box size, x_n is the original coordinate of a n-th particle, and $x_{\mathcal{P}_n}$ is the destination coordinate some "time" τ later and after invoking the periodic boundary conditions [12, 13]. If they have not been invoked, the difference in Eq. 2.46 is zero, and if they have been invoked multiple times, the results also multiply. Essentially, the winding number calculates the net number of times particle "paths" have wound around the periodic unit cell. Generally, the winding number is a vector, containing components for each dimension of a system with periodic boundary conditions. Also, it is important to note that Eq. 2.46 defines the winding number as an integer, so it is quantized. This topic will be revisited in section 3.2.3.

The distribution of winding numbers W in 1D is given by the expression [13]:

$$P(W) = \frac{e^{-W^2 \pi LT/2\hbar v_J}}{\vartheta_3 \left(0, e^{-\pi LT/2\hbar v_J}\right)}, \tag{2.47}$$

where $\vartheta_3(z, q)$ is Jacobi theta function of third order. Finite superfluid response is possible only when the oscillations of the field φ are suppressed, and in turn $\langle J \rangle \approx 0$ [13]. In 1D, superfluid density[2] ρ_s/ρ, is directly proportional to the second moment of distribution of winding numbers [12]:

$$\frac{\rho_s}{\rho} = \frac{\pi LT}{\hbar v_J} \left\langle W^2 \right\rangle. \tag{2.48}$$

Thus, introducing Eq. 2.47 to relation for the superfluid fraction in Eq. 2.48 we obtain [14]

$$\frac{\rho_s}{\rho} = \frac{\pi LT}{4\hbar v_J} \frac{\left|\vartheta_3'' \left(0, e^{-\pi LT/2\hbar v_J}\right)\right|}{\vartheta_3 \left(0, e^{-\pi LT/2\hbar v_J}\right)}, \tag{2.49}$$

where $\rho = \rho_s + \rho_n \equiv \rho_0$ is total density and $\vartheta_j''(z, q) \equiv \partial_{xx}^2 \vartheta_j(z, q)$. In Eqs. 2.47, 2.48 and 2.49, $k_B = 1$ was used.

This theoretical prediction will be used as a model function for further studies of the superfluid density. For now, keep in mind that the expressions in both Eq. 2.47 and Eq. 2.49 are scaling functions of the product LT, and not box length L or temperature T individually, and since Luttinger parameters are insensitive to temperature and finite-size effects, they must be fixed and valid for any L and T of the low-energy theory [8].

---

[2]Not to be confused with the smeared density ρ_S in Eq. 2.34.

3 Method

This chapter will present the development of theoretical concepts of Path Integral formalism of quantum mechanics into the computational algorithm called Path Integral Monte Carlo (PIMC). A general approach to the Monte Carlo method of stochastic computation will be described and the way to implement PI formulation to it, as well as a unique way to sample the permutation space of quantum objects, called the *worm* algorithm. Since the simulations of physical systems generally require approximations to function more efficiently, a section of this chapter will be dedicated to the approximations for kinetic and potential action and the estimators used to calculate the physical properties. Finally, the code for the algorithm, written in C++, will be briefly reviewed.

3.1 Path Integral Monte Carlo simulations

Two major contemporary methods of simulating physical systems are molecular dynamics, which relies on application of Newton's equations to present real-time motion of classical particles, and the stochastic computation method well known as Monte Carlo, which is based around generating random numbers according to various probability distribution functions that are often used for calculations of multidimensional integrals. The later method is almost essential for any kind of simulations regarding quantum systems. The basic goal of our simulations is to evaluate the integral in Eq. 2.20 in order to know elements of the thermal density matrix $\widehat{\rho}$ and therefore all the quantities of the thermal system derived from it. To understand the simulation process itself, it is necessary to have an insight into the way that Monte Carlo methods work and how they can reproduce the desired solutions.

3.1.1 Monte Carlo methods

Monte Carlo is a widely known term for a broad class of computational methods that rely on stochastic sampling to obtain numerical results. The core of every Monte Carlo algorithm is the usage of random numbers, done in order to create a certain probability distribution specific to the problem at hand. These methods have found use in many areas and disciplines, including economics, computer graphics, visual design and of course, science. They are of particular value for the calculation of multidimensional integrals in systems with a large number of degrees of freedom.

Suppose we have a system[3] consisting of infinite number of states μ, each with some

---

[3]The system need not be physical at all. For this reason, links to the actual physical applications will be avoided for a few paragraphs, although the scientific approach might be simpler for understanding.

weight ω_μ, and we want to calculate the average of some quantity F. The average is

$$\langle F \rangle = \sum_\mu \omega_\mu F_\mu, \tag{3.1}$$

where $\sum_\mu \omega_\mu = 1$. The problem with this sum is that it consists of infinite number of elements, which is quite often impossible to calculate analytically. One useful approach in its evaluation is to calculate the sum in Eq. 3.1 numerically. This method is approximative, for it necessarily reduces the summation to a finite number of components, but it can still be quite effective and precise in determining the value of $\langle F \rangle$ [5]. For better results, a large enough number of elements is needed to ensure the convergence of the average.

To calculate the averages of finite number M of system states μ with weights ω_μ and sampled according to the probability p_μ we use the formula

$$\langle F \rangle = \frac{\sum_{\mu=1}^{M} \omega_\mu p_\mu^{-1} F_\mu}{\sum_{\mu=1}^{M} \omega_\mu p_\mu^{-1}}, \tag{3.2}$$

which is derived from the central limit theorem. Obviously, the choice of probability distribution p_μ, from which we are sampling our configuration, strongly affects the efficiency of this calculation. One approach is to sample the states according to the uniform random distribution over the domain of states. However, it is often the case that only a small number of states contributes strongly to the averages, while the rest influence it with negligible contributions. An example a case like this is the Boltzmann distribution $p_\mu = Z^{-1} e^{-\beta E_\mu}$ [5]. If we are not able to effectively produce the probability distribution specific to our problem, the calculation will converge slowly because too much computational time will be wasted on the states with small contributions. For this reason, methods of *importance sampling* have been developed. This process consists of selectively accepting the contributions of certain states in accordance with the desired probability distribution.

One of such schemes of importance sampling is called Metropolis algorithm [5, 15, 16]. It is based around the idea of sampling a "more likely" regions of phase space - the ones with the higher probability density. The Metropolis algorithm is essentially a Markov chain - a sequence of stochastic events created to produce some probability distribution, in which every event depends only on the previous one, and not the entire chain of events. The evolution of such a process, represented by $\Pi(\mu_i \to \mu_{i+1})$, where μ_i and μ_{i+1} are two consecutive states in the chain of events, satisfies the detailed balance condition

$$\Pi(\mu_i \to \mu_{i+1}) \, p(\mu_i) = \Pi(\mu_{i+1} \to \mu_i) \, p(\mu_{i+1}). \tag{3.3}$$

This is the only condition, which gives us some freedom in choosing $\Pi(\mu_i \to \mu_{i+1})$. For convenience, we can separate the process into a composition of two subprocesses [5]

$$\Pi(\mu_i \to \mu_{i+1}) = C(\mu_i \to \mu_{i+1}) \, T(\mu_i \to \mu_{i+1}), \tag{3.4}$$

where $C(\mu_i \to \mu_{i+1})$ is the change we make to the state μ_i to advance it to the state μ_{i+1} and $T(\mu_i \to \mu_{i+1})$ represents the means of calculating the probability of accepting

or not accepting that change. In general, C is arbitrary, while T is calculated from C to satisfy the detailed balance condition in Eq. 3.3. If C is chosen to also satisfy the detailed balance, then T can be calculated from the formula [5, 15, 16]

$$T\left(\mu_i \to \mu_{i+1}\right) = \min\left[1, \frac{p(\mu_{i+1})}{p(\mu_i)}\right].$$ (3.5)

The Metropolis algorithm can be used in evaluation of averages that have the form

$$\langle F \rangle = \frac{\int F(x)p(x)\mathrm{d}x}{\int p(x)\mathrm{d}x}.$$ (3.6)

Here, $p(x)$ is the desired probability distribution function, the variable x can represent any number of degrees of freedom and the integration is carried out over the domain of possible inputs for x. In a numerical evaluation, the average can be calculated statistically [15, 16]:

$$\langle F \rangle = \frac{1}{M}\sum_{\mu=1}^{M} F(x_\mu),$$ (3.7)

where the points x_μ are sampled according to $p(x)$. The purpose of this method is to calculate the integral in numerator of Eq. 3.6, which is precisely the form of the integral in Eq. 2.16.

The process of the algorithm consists of several steps:

1. Propose a trial state $\mu_{trial} = \mu_i + \delta_i$, where δ_i is a random value selected according to the uniform distribution from the interval $[-\delta, \delta]$. This represents the change C in the stochastic process.

2. Calculate the number $\alpha = \frac{p(\mu_{trial})}{p(\mu_i)}$, a ratio of trial and initial probability.

3. Accept the transition to the trial state with probability α. This represents the calculation of probability in Eq. 3.5 , and includes the following:

   a) if $\alpha \geq 1$, then accept the movement, $\mu_{i+1} = \mu_{trial}$

   b) if $\alpha < 1$, generate a random number $r \in [0, 1\rangle$

   c) if $r \leq \alpha$, accept the movement, $\mu_{i+1} = \mu_{trial}$

   d) if $r > \alpha$, discard the movement, that is, keep the system in the initial state: $\mu_{i+1} = \mu_i$

4. Repeat to generate the chain of events μ_{i+2}, μ_{i+3}, ...

This algorithm can sample any probability distribution, but it is not without flaws. Firstly, the results are correct only asymptotically and secondly, two consecutive states in the Markov chain are strongly correlated with each other.

To overcome the first issue, one needs to allow the equilibration of the system. When the system has reached it's asymptotic regime, we discard the certain number of initial

states from the calculation of averages. There is no analytical way to do this, however. Usually, the user just observes the calculated observables to the point at which the system no longer fluctuates and decides manually to ignore a number of initial results. This method is rather robust because it relies on a human factor and can't account for possible metastable states in the asymptotic regime, but works sufficiently well for large enough simulations.

The second problem is relevant for the calculations of statistical errors of the averages. It can be resolved with *data blocking* method [5]. It consists of separating a sequence of M calculated values into m smaller groups of data, each consisting of $K = \frac{M}{m}$ values. By averaging the calculated data (which is the estimates of the observables) inside groups, we get K values of averages of observables, F_j. The average of those F_j is independent of m and is still an estimate of the actual average $\langle F \rangle$. If K is large enough, data groups can be considered as statistically independent and we can calculate the errors using the formula

$$\sigma_F = \sqrt{\frac{1}{m(m-1)} \sum_{j=1}^{m} (F_j - \langle F \rangle)}. \tag{3.8}$$

Finally, one last way to accelerate the convergence of the values to the asymptotic regime is connected to the size of proposed updates to the states δ_i. If the updates are too large and they considerably shift the configuration of the system, then most of them will be rejected since they will transition the system into states with lower probability density. This will cause the process to converge slowly towards the wanted probability density. On the other hand, if the updates are very small, they will keep the system in the region of high probability density without exploring the regions of lower probability density, which can impair the ergodicity of the system and produce incorrect values of observable averages. A good compromise between these two cases is to keep the acceptance rate at about 50%, which is done by dynamically adjusting the interval $[-\delta, \delta]$ based on the aggregated acceptance rate [5].

3.1.2 Path Integral implementation of Metropolis algorithm

The scheme described in the previous section can be used to calculate the value of integrals and averages defined by the Path Integral formulation for thermal quantum systems. The goal of our simulaions is to reliably sample the probability density to determine the physical quantities of a system at finite temperature T. We are simulating a canonical ensemble; the system is at constant finite volume Ω and with constant number of particles N. To this end, we will revisit the classical mapping of a quantum system in imaginary time, presented in section 2.1.3.

The system consists of N particles with paths in imaginary time. We discretize the imaginary time dimension of classical space into M parts. This way, every quantum particle is split into M beads, which are equivalent to classical particles of a ring polymer, connected through imaginary time with kinetic action spring propagators and interacting with coordinate-dependent potential action inside a single time slice. The schematic

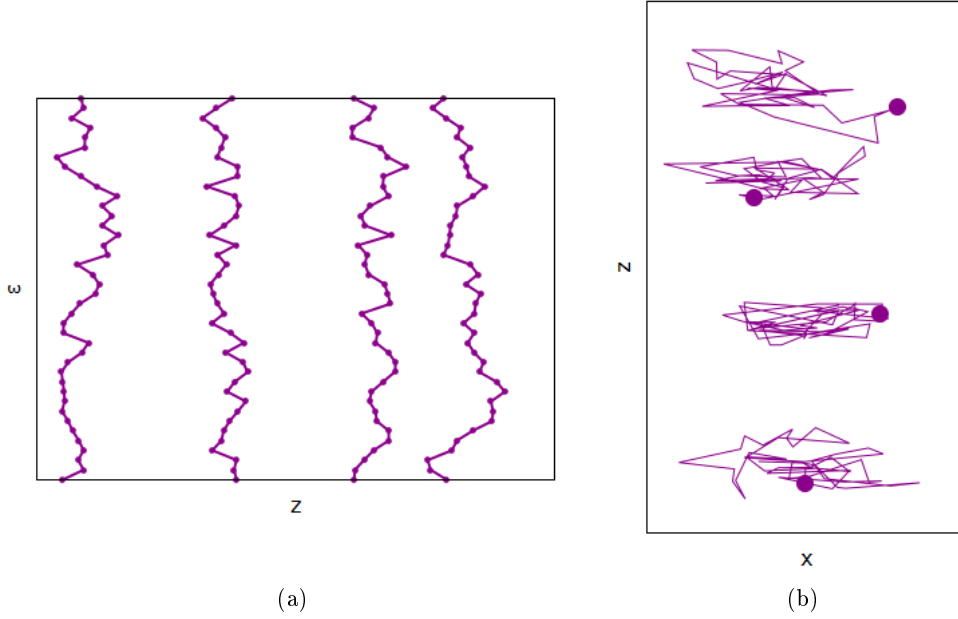(a)   (b)

Figure 3.1: World line example of particle paths in imaginary time. Every bead of an individual particle is connected with lines to the previous and the next bead, with respect to the time slice. (a) Particle z coordinates are presented in dependance of imaginary time value ϵ. Individual beads are marked by dots. (b) Paths that the particles form, plotted in $x - z$ plane. Because of the periodic boundary condition for imaginary time dimension, they form closed polymers. Large circles represent initial and final beads.

representation of this system is shown in Fig. 3.1. This portrayal of the paths is called the *world-line* representation.

In section 2.1.2, convolution property of the density matrix was described, leading to the Eq. 2.20 and in accordance with discretization of imaginary time, $\epsilon = \frac{\beta}{M}$. This can be used to calculate the average of any observable F, following the example presented in Eq. 2.16. These expectation values can then be written as [5]

$$\langle F \rangle = \int \prod_{j=1}^{M} \mathrm{d}\mathbf{R}_j F(\mathbf{R}_j) \widehat{\rho}(\mathbf{R}_j, \mathbf{R}_{j+1}; \epsilon). \tag{3.9}$$

This is exactly the form of integrals found in Eq. 3.6 that the Metropolis algorithm is best used to solve. It is important to highlight that the presence of partition function Z in the definition of density matrix in Eq. 2.12 makes it normalized.[4] Combined with the fact that every element of the density matrix is positive definite in the coordinate

---

[4]In some literature, the density matrix is purposely defined not divided by the partition function, and thus not normalized.

representation, we can interpret

$$p(\mathbf{R}_1, ..., \mathbf{R}_M) = \prod_{j=1}^{M} \widehat{\rho}(\mathbf{R}_j, \mathbf{R}_{j+1}; \epsilon) \tag{3.10}$$

as probability density [5]. Then, the integral in Eq. 3.9 is suitable for evaluation by Monte Carlo method. One must sample all the degrees of freedom $\mathbf{R}_1$, $\mathbf{R}_2$, ..., $\mathbf{R}_M$ according to this probability density and simply statistically calculate the averages of observables.

Having the classical representation in mind, it is viable to construct a Metropolis algorithm implementation of Path Integral formulation, that is, of the bead-polymer model. The steps of this procedure are as follows:

1. Initiate the coordinates of all beads of all particles. This constructs the initial paths in imaginary time. One common practice for this is to have all the beads of a single particle at the same coordinate, making the world line picture just straight lines, and place particles on a lattice or randomly, depending on the system one is simulating.

2. Pick one bead (of any particle) at random and propose a new position. This is shown in Fig. 3.2.

3. Accept this movement with probability

$$T(\mathbf{R}_{initial} \rightarrow \mathbf{R}_{trial}) = \min\left[1, \frac{\widehat{\rho}_{trial}}{\widehat{\rho}_{initial}}\right]. \tag{3.11}$$

   Since moving a single bead changes the kinetic action only between the previous and the next bead and potential action of only a single time slice, only those contributions will affect the trial and initial density matrix ratio.

4. Calculate the averages of physical observables in the fashion of Eq. 3.9.

5. Go back to step 2.

To calculate the quantities more accurately and accelerate the convergence to the desired probability density, proper approximations for action and the density matrix are needed. These approximations often rely on the fact that the imaginary time step ϵ is small enough to neglect higher orders of the expansion. They will be reviewed in the next section, but for now let us consider that, for small enough ϵ, Lagrangian can be evaluated as [16]

$$L = -\frac{m}{2}\left(\frac{\Delta x}{\epsilon}\right)^2 - V(x) = -E. \tag{3.12}$$

Since this is a time-independent constant, using the definitions from Eq. 2.12 and Eq. 2.22, we can rewrite the density matrix as

$$\widehat{\rho}(\mathbf{R}_m, \mathbf{R}_{m+1}; \epsilon) = Z^{-1}e^{-S} = Z^{-1}e^{-\epsilon(\widehat{K}+\widehat{V})}. \tag{3.13}$$
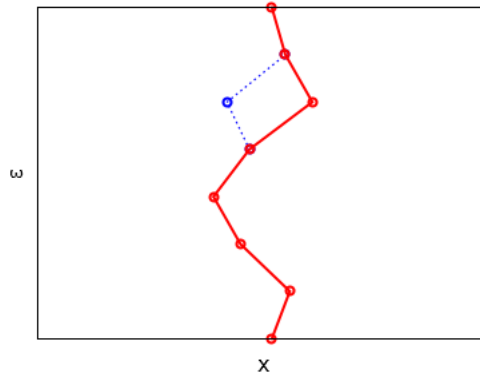
Figure 3.2: Single bead update of a single particle polymer, presented in one spatial dimension x. The old path and the new path differ in one bead, red for the new path and blue for the old. The update is accepted according to the scheme presented in section 3.1.1.

It is clear that the density matrix actually has the form of an imaginary time action propagator. Furthermore, the density matrix ratio in Eq. 3.11 is actually defined by the probability density in Eq. 3.10 for different sets of configurations. This ratio is well illustrated with $\exp(-S_{trial})/\exp(-S_{initial})$ [5]. Since the density matrix convoluted product represents probability density, by operating with Metropolis algorithm, we are also sampling paths with more likely action, the most likely being the classical action. This shows that the PIMC algorithm inherently implements the minimization of action - Hamilton's principle, in quantum mechanics.

Although the results are always approximate because the M is finite, it is possible, for large enough M, to reduce the systematic errors so much that they are lower than the inevitable statistical errors attributed to the Monte Carlo procedure. Because of this, virtually exact averages of observables $\langle F \rangle$ can be recovered, practically in the $M \to \infty$ limit. Therefore, the Path Integral Monte Carlo method is often considered the *exact* computational method [1, 5].

3.1.3 Worm algorithm

The Metropolis scheme for path integral formulation described in the previous section is actually effectively flawed for quantum particles. While the principle is admissible for sampling the systems efficiently, it still requires a very relevant fine-tuning to be applicable to a wider variety of physical systems. The most prominent flaw in this remark is the inability to sample different permutations of quantum particles.

This is where the analogy with the classical system fades - to sample all the possible permutations of a quantum system, one must sample many different classical systems of bead polymers, the differences being links between beads. Particle exchange is represented by changing the kinetic action link to another particle, as portrayed in Fig. 3.3. While this is not unordinary for a quantum system, the classically isomorphous one
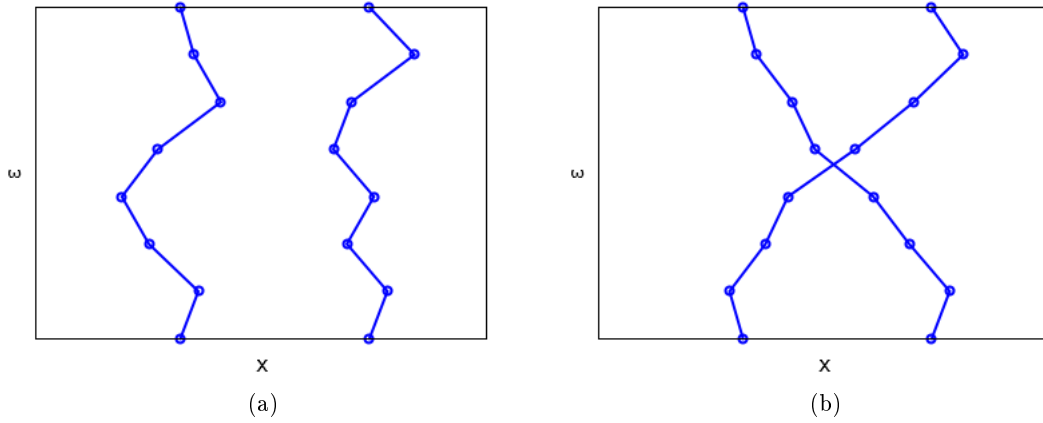
Figure 3.3: An example of possible system transition representing particle exchange. Since quantum particles do not have identities, exchanges are possible with any particle of the same kind. This translates into the world line picture as change of the kinetic link from one particle-polymer to the other, which may result in polymers creating a tangled weave of connections. The end beads in both (a) and (b) are the same because of the $\mathbf{R}_1 = \mathbf{R}_{M+1}$ boundary condition.

becomes something else entirely, with the possibility of intertwining, connected polymers.

So far, we have described a scheme that would sample only a single permutation of particles. When we include additional permutations, we must deal with the fact that quantum states, and therefore the density matrix, must be either symmetric or antisymmetric to the permutation. One convenient way to define $\widehat{\rho}$ in accordance with this is to sum all density matrices of all possible permutations:

$$\widehat{\rho}_{full}(\mathbf{R}_1, \mathbf{R}_2; \epsilon) = \frac{1}{N!} \sum_{\mathcal{P}} (\pm 1)^P \, \widehat{\rho}(\mathbf{R}_1, \mathcal{P}\mathbf{R}_2; \epsilon) \tag{3.14}$$

where $\mathcal{P}$ is one of the $N!$ possible permutations of N particles, and P is the number of transpositions in a given permutation. In the (± 1) term, the $+$ sign is chosen when dealing with Bose-Einstein statistics, and $-$ sign for Fermi-Dirac statistics. Using this definition, the way observable averages in Eq. 3.9 are calculated must be updated [5]:

$$\langle F \rangle_{full} = \frac{1}{N!} \sum_{\mathcal{P}} \int \prod_{j=1}^{M} \mathrm{d}\mathbf{R}_j F(\mathbf{R}_j) \, (\pm 1)^P \, \widehat{\rho}(\mathbf{R}_j, \mathcal{P}\mathbf{R}_{j+1}; \epsilon). \tag{3.15}$$

Fortunately, this changes nothing in Eq. 3.10 and Metropolis algorithm can still be applied using the updated density matrix to define the probability density. Sampling over all the possible permutations must be included. A scheme to sample the permutations directly has been developed, but clearly the direct sampling becomes impractical with the

increase of number of particles. Additionally difficulties of PIMC algorithm are that for some systems, single bead updates can simply never be enough to efficiently sample the whole configuration space. For example, systems consisting of very heavy particles have a very low probability of accepting a single bead move. Thus, different moves must be implemented, consisting of updating larger segments of polymers, or even whole polymers at the same time, or changing links between polymers to sample different permutations.

An efficient method of sampling was developed to this end, called the *worm algorithm* (WA) [17, 18]. It introduces a new set of moves that update the system, each accepted in accordance with the Metropolis algorithm scheme. These moves bring the system to an expanded ensemble, containing one more particle within a polymer called the *worm*. This ensemble is still canonical, at temperature T and with volume Ω, just with one additional particle in one time slice, which effectively makes the polymer open. Of course, the $\mathbf{R}_1 = \mathbf{R}_{M+1}$ condition must still be satisfied if we want to compute the average values of diagonal observables, so the system must return to the regular ensemble with N particles. This expanded ensemble will be called *G-sector*, while the regular ensemble will be called *Z-sector* [5, 17]. *G*-sector contains one open world line; that is, two unconnected beads of the worm. Last time slice and first time slice beads of the worm are called the *head* and the *tail* respectively, or historically *Masha* and *Ira* [17, 18].

New moves introduced by the worm algorithm can be divided into 3 groups, by the nature of updates. Firstly, there are updates performable in both Z and G-sector: Translate and Staging. These updates do not sample different permutations of particles and are enough to ensure ergodicity in systems where permutations can be ignored. Such types of updates also existed in the conventional PIMC algorithm [1].
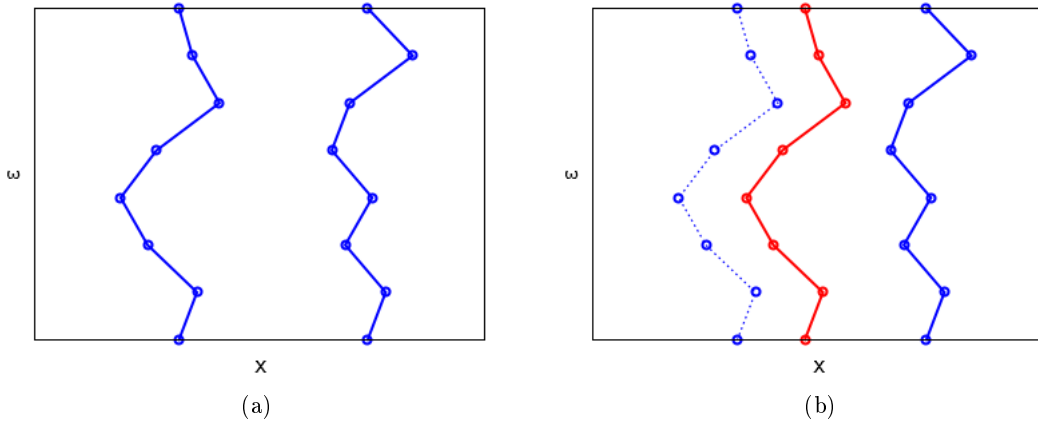

Figure 3.4: Translate movement of the worm algorithm, shown schematically in one dimension. Here, (a) shows old configuration, and (b) shows new, with the translated polymer colored red and previous configuration in dashed lines.

- **Translate (displace)** [5]. This update moves the entire polymer as a rigid body, not changing the links between it's beads. We select a particle index i at random
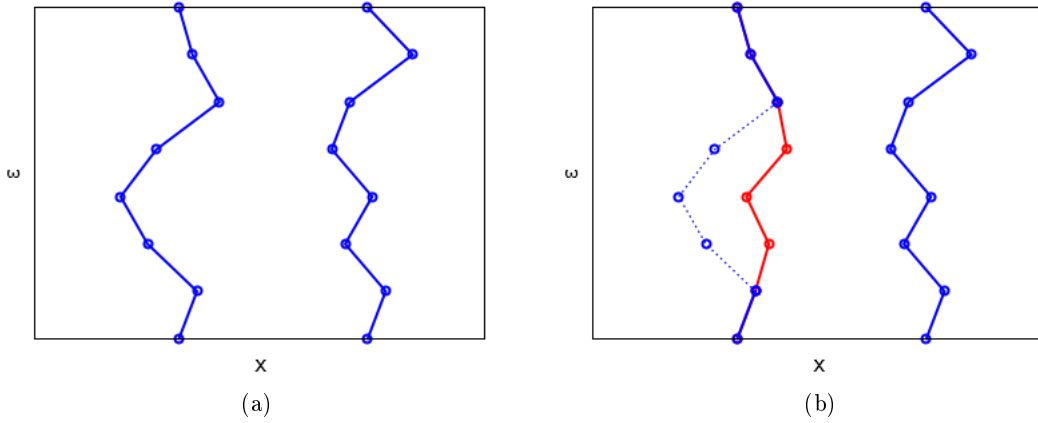
Figure 3.5: Staging movement of the worm algorithm, shown schematically in one dimension. Here, (a) shows old configuration, and (b) shows new, with the redrawn polymer segment colored red and previous configuration of that segment in dashed lines.

and a movement vector $\Delta \mathbf{r} = (\Delta x, \Delta y, \Delta z)$, whose coordinate values are selected from a predetermined interval. We move every bead j of the selected polymer i as $\mathbf{r}_{i,j} \rightarrow \mathbf{r}'_{i,j} = \mathbf{r}_{i,j} + \Delta \mathbf{r}$. Since links are not changed, this move does not change the kinetic energy of the system, so it can be safely avoided in movement probability evaluation. This move is shown in Fig. 3.4.

- **Staging** [5] (**wiggle** [19]). This update recreates a segment of the selected polymer between two beads fixed distance apart. We start by selecting a random polymer with index i and a random bead j_0 belonging to that polymer. Beads j_0 and j_{0+l} are kept fixed, where $l < M$ is the integer distance determined by input. We assign new values to coordinates of every bead in between[5]. This move is schematically shown in Fig. 3.5.

The second group of movements switches configurations back and forth between Z-sector and G-sector: Open and Close. To satisfy the detailed balance condition, both of these updates must happen - that is, if a polymer has been opened, it must also be closed to return the system into diagonal configuration.

- **Open** [17, 18]. This update creates two extremities from an existing polymer. It can only be done while the system is in Z-sector and brings the system to G-sector configuration. We randomly select a particle index i, one of its random beads j and an integer $l \in [1, l_{max}]$, where $l_{max} < M$ is predetermined. Then, $l - 1$ beads are removed, starting from j-th. This leaves us with an unconnected segment of the polymer, with $\mathbf{r}_{i,j}$ bead being the tail, and $\mathbf{r}_{i,j+l}$ the head of the newly created

---

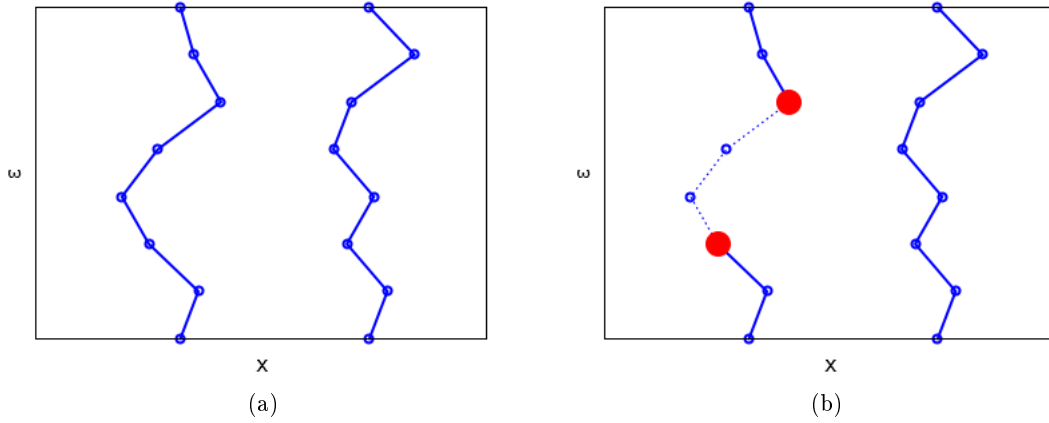[5]Detailed description of how this is done can be found in Refs. [5, 19].

Figure 3.6: Open movement of the worm algorithm, shown schematically in one dimension. Here, (a) shows old configuration, and (b) shows new, with the removed segment of the polymer in dashed blue lines and head and tail of the worm as filled red dots.

worm. If this update is accepted, we denote the polymer as worm, changing the index to i_W. This movement is represented in Fig. 3.6.

- **Close** [17, 18]. This update closes an open polymer, removing the worm from the system. It can only be done in a G-sector configuration and brings the system to Z-sector. The head and the tail of the worm are $l \in [1, l_{max}]$ beads apart, where $l_{max} < M$ is the same algorithm parameter as in Open movement. We reconstruct the $l-1$ beads long segment from the tail bead $\mathbf{r}_{i_W, j}$ to the head $\mathbf{r}_{i_W, j+l}$, previously unconnected. This is done with the product of l free particle propagators, one for each new link to be reconstructed. If the movement is accepted, the system returns to a diagonal Z-sector configuration. This update is shown in Fig. 3.7.

The third group consists of movements performed only in G-sector: Advance, recede and Swap. Among them, Swap is of special importance interest since it accounts for particle permutation sampling.

- **Advance** [17, 18]. This update propagates the tail of the worm by a random number of time slices forward. We select a random number $l \in [1, l_W]$ of beads to be constructed, where $l_W \leq l_{max} < M$ is the current number of unconnected beads between the tail and the head of the worm, and l_{max} is the same maximum worm length parameter as in Open and Close. Then, starting from the tail bead $\mathbf{r}_{i_W, j}$, we reconstruct l beads forward in time and the links between them with the free particle propagator. If accepted, this update makes the bead $\mathbf{r}_{i_W, j+l}$ new tail of the worm. Advance will never be able to close the polymer and thus remove the worm. This is schematically shown in Fig. 3.8.
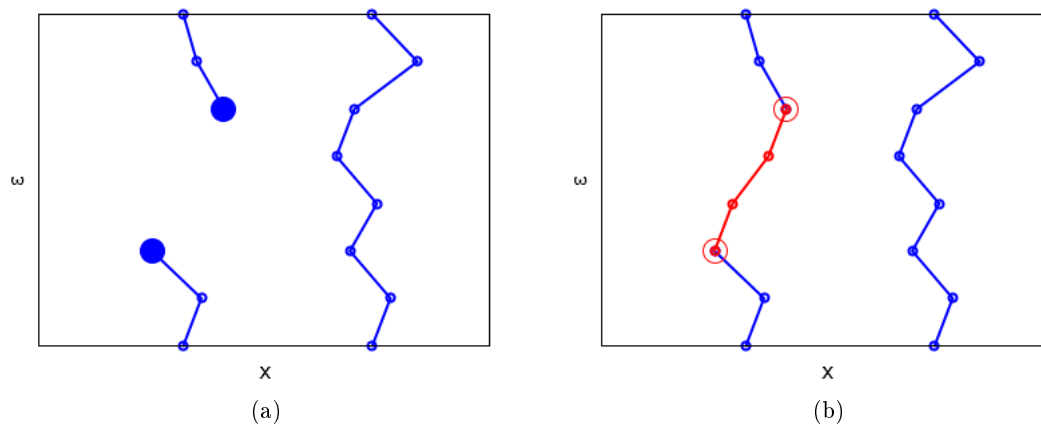
Figure 3.7: Close movement of the worm algorithm, shown schematically in one dimension. Here, (a) shows old configuration, with the head and the tail as fileld blue dots, and the (b) shows new configuration, with the segment that completes the closed polymer colored red and the former head and tail as blank red dots.

Figure 3.8: Advance movement of the worm algorithm, shown schematically in one dimension. Here, (a) shows old configuration, with the head and the tail as filled blue dots, and the (b) shows new configuration, with the newly constructed segment in red lines, new head as filled red dot and old head as blank red dot.

- **Recede** [17, 18]. This movement removes a number of beads from the tail, effectively pushing the tail back backwards in time. We select a random number $l \in [1, M]$ of beads to be deleted. Starting with the tail bead $\mathbf{r}_{i_W, j}$, we remove l

beads back, thus making the bead $\mathbf{r}_{i_W,j-l}$ a new tail of the worm. If accepted, this movement increases the length of the worm by l. Recede will not be accepted if it deletes the entire length of the open polymer. This update is shown in Fig. 3.9.
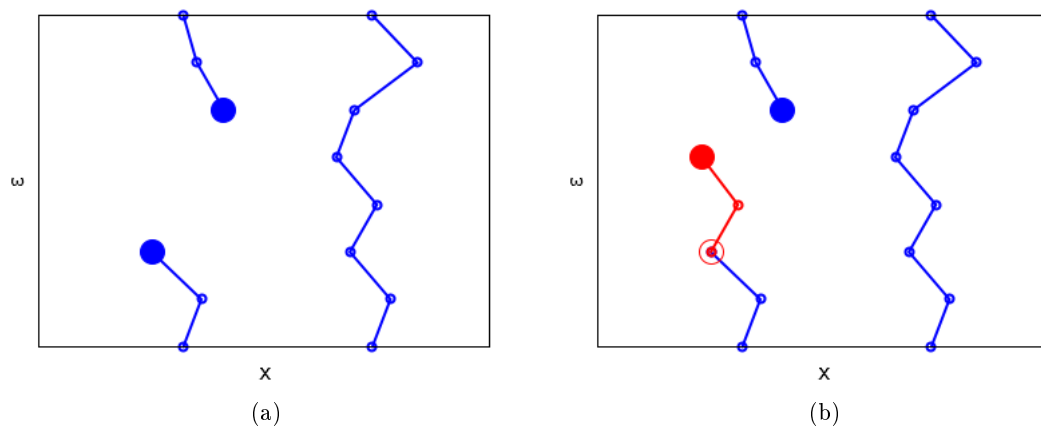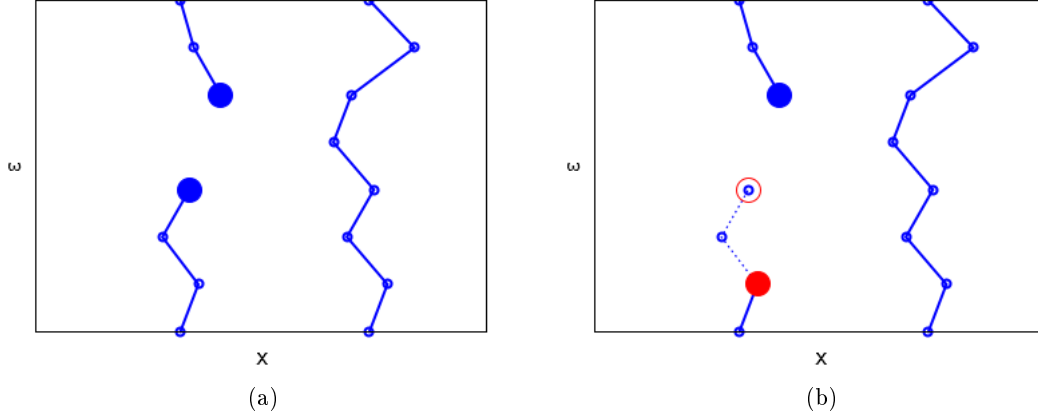

<center>(a)</center>

<center>(b)</center>

Figure 3.9: Recede movement of the worm algorithm, shown schematically in one dimension. Here, (a) shows old configuration, with the head and the tail as filled blue dots, and (b) shows new configuration, with the removed segment in dashed blue lines, the head as filled blue dot, former tail of the worm as blank red dot and new tail as the filled red dot.

- **Swap** [5, 17, 18]. This update recreates the links between different polymers of the same particle type (i.e. identical particles), thus performing particle permutations. It can only be done in G-sector since it requires the presence of the worm. We start by randomly selecting an integer $l \in [1, l_{max}]$, which is the number of beads the update will reconstruct, and $l_{max} < M$ being determined by input. Next, we compute the following quantity for each particle i:

$$\Pi_p(i) = \sqrt{\frac{m}{2\pi\hbar^2 l\epsilon}} \exp\left[-\frac{m}{2\pi\hbar^2 l\epsilon}(\mathbf{r}_{i,l+1} - \mathbf{r}_{i_W,M+1})^2\right], \qquad (3.16)$$

and also

$$\Sigma_W = \sum_{i=1}^{N} \Pi_p(i). \qquad (3.17)$$

Then, we select a particle index i_K with the probability $\Pi_p(i_K)/\Sigma_W$. This polymer represents the reconstruction partner of the worm and the main idea is to remake a path between the tail of the worm $\mathbf{r}_{i_W,j}$ and the bead $\mathbf{r}_{i_K,j+l}$. We recreate the path between these two beads with the free particle propagator, similar to Close movement, and remove beads $\mathbf{r}_{i_K,j+1}$, $\mathbf{r}_{i_K,j+2}$, ..., $\mathbf{r}_{i_K,j+l-1}$. It is important to ensure that this update does not bring the system into a Z-sector configuration and that it satisfies the detailed balance condition. If so, and if the update is

accepted, tail of the worm has moved from $\mathbf{r}_{i_W,j}$ to $\mathbf{r}_{i_K,j}$ and the links between polymers have been modified. Note that this move does not change the length of the worm. This move is schematically shown in Fig. 3.10.

All of the mentioned input parameters can be modified to accelerate the convergence rate of the algorithm. These updates provide scheme that can successfully sample permutations of particles and a wide variety of systems, all of which the original PIMC algorithm was lacking.
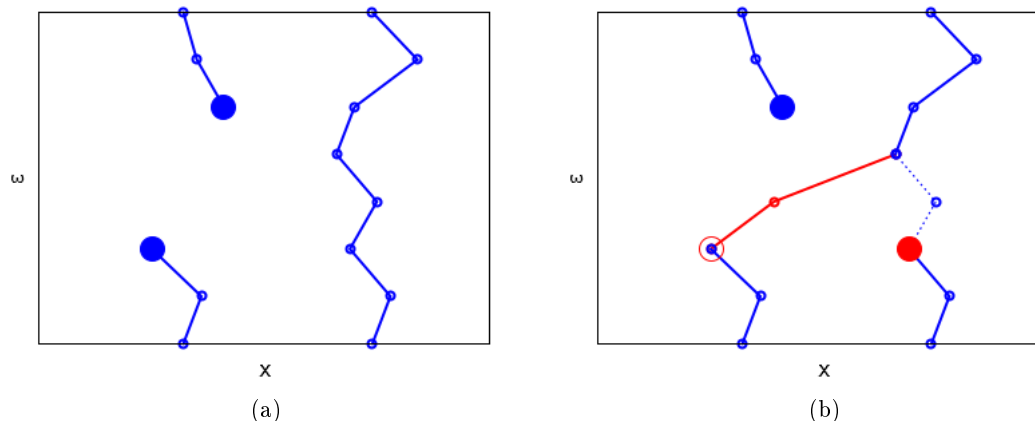

Figure 3.10: Swap movement of the worm algorithm, shown schematically in one dimension. Here, (a) shows old configuration, with the head and the tail as filled blue dots, and the (b) shows new configuration, with the new segment that that connects the previously unconnected tail of the worm to the new polymer colored red, previous part of the reconstruction partner in dashed lines, former tail as blank red dot, new tail as fileld red dot and the unchanged head as filled blue dot. The system is still in an off-diagonal G-sector configuration, with a changed tail of the worm.

3.2 Approximations and estimators

The major concern of this section is computational efficiency. In simulations of physical systems, most important matters are speed of the calculation and accuracy of the results, and successfulness of a simulation is often a question of balancing the former and the later. To accelerate the computation, one must provide a suitable approximations for *ab initio* definitions of basic physical quantities. In this case, that is kinetic and potential action. Furthermore, to ensure the results are precise enough, one must develop a way to calculate all the desired properties from available information. In some cases, it is more convenient to use a statistical estimator rather that the definition, and sometimes there are even multiple estimators for a single property.

3.2.1 Action approximations

We have already observed a close relation between action and the density matrix, most obvious being in the form of Eq. 3.13. However, this sum of potential and kinetic action in the exponential operator is not so straightforward to evaluate as it may seem. Since in the classical isomorphism of PIMC algorithm, it is stated that potential action acts on the beads within only the same time slice, and kinetic action acts between neighboring beads of the same particle imaginary-time-wise, it is desirable to separate potential and kinetic action in different expressions. This means that the exponential operator in Eq. 3.13 must be expanded in the terms of imaginary time ϵ. This expansion is called the Baker-Campbell-Hausdorff formula:

$$e^{-\epsilon(\widehat{K}+\widehat{V})} = e^{-\epsilon\widehat{K}}e^{-\epsilon\widehat{V}}e^{-\frac{\epsilon^2}{2}[\widehat{K},\widehat{V}]}e^{-\frac{\epsilon^3}{6}\left(2[\widehat{V},[\widehat{K},\widehat{V}]]+[\widehat{K},[\widehat{K},\widehat{V}]]\right)}\ldots \qquad (3.18)$$

This expression also has a convergence property described by the Trotter formula [5]:

$$e^{-\beta(\widehat{K}+\widehat{V})} = \lim_{M\to\infty}\left(e^{-\epsilon\widehat{K}}e^{-\epsilon\widehat{V}}\right)^M. \qquad (3.19)$$

This means that it is possible to give a suitable approximation based on the order of imaginary time. Since the relation between imaginary time ϵ and temperature T is reciprocal, the lower the order of ϵ, the higher the temperature and the number of time slices M for the approximation.

The lowest approximation for the action is the one in the limit of very small imaginary time ϵ. All the elements of the expansion Eq. 3.18 of order ϵ^2 or higher happen to contain commutators of kinetic and potential action and this approximation makes it that more convenient to neglect them. Combining this with equations 2.18 and 3.13, the density matrix then becomes

$$\widehat{\rho}\left(\mathbf{R}_1,\mathbf{R}_2;\epsilon\right) = \frac{1}{Z}\int d\mathbf{R}' \left\langle\mathbf{R}_2|e^{-\epsilon\widehat{K}}|\mathbf{R}'\right\rangle \left\langle\mathbf{R}'|e^{-\epsilon\widehat{V}}|\mathbf{R}_1\right\rangle. \qquad (3.20)$$

This is called the *primitive approximation* [5, 20]. It enables simple calculation of matrix elements of operators $e^{-\epsilon\widehat{K}}$ and $e^{-\epsilon\widehat{V}}$ in coordinate representation. The kinetic operator can be calculated exactly, from the definition Eq. 2.24. In coordinate representation, the matrix element is

$$\left\langle\mathbf{R}_{m+1}|e^{-\epsilon\widehat{K}}|\mathbf{R}_m\right\rangle = (4\pi\lambda\epsilon)^{-\frac{dN}{2}}e^{-\frac{(\mathbf{R}_{m+1}-\mathbf{R}_m)^2}{4\lambda\epsilon}}, \qquad (3.21)$$

where d is the dimensionality of the system, and $(\mathbf{R}_{m+1}-\mathbf{R}_m)^2 = \sum_{i=1}^{N}(\mathbf{r}_{i,m+1}-\mathbf{r}_{i,m})^2$ abbreviation is used. Potential operator is simple to evaluate because it is diagonal in the coordinate representation. The matrix element is

$$\left\langle\mathbf{R}_{m+1}|e^{-\epsilon\widehat{V}}|\mathbf{R}_m\right\rangle = e^{-\epsilon V(\mathbf{R}_m)}\delta(\mathbf{R}_{m+1}-\mathbf{R}_m). \qquad (3.22)$$

Here, we have used $V(\mathbf{R}_m) = \sum_{i'<i''}v(\mathbf{r}_{i',m}-\mathbf{r}_{i'',m})$ as definition of total potential within a single time slice with index m, where $v(\mathbf{r}_{i',m}-\mathbf{r}_{i'',m})$ is the pair potential

between individual particles with indices i' and i'', such that the total potential part of the Hamiltonian is $V = \sum_{i<j} v(\mathbf{r}_i - \mathbf{r}_j)$.

Of course, the primitive approximation is only accurate to order ϵ^2, which makes the convergence to the exact values slow. It is suitable for systems in which the quantum effects are not very pronounced, but a more accurate and reliable approximation of the higher order is needed for more complex systems studies, such as Bose-Einstein condensation and superfluidity properties that we are dealing with in this work. The higher order of the approximation also means more computational complexity, so it is important that, along with accuracy, efficiency of the developed scheme exceeds the primitive approximation.

Starting with Baker-Campbell-Hausdorff formula in Eq. 3.18, one could develop an approximation of second or higher order. However, it has been shown that expansions to the second or higher order tend to produce non-Hermitian effects [5]. Still, since we are interested in thermodynamic properties of the system, non-Hermitian results can be tolerated as long as we only take the trace of the thermal density matrix in account.

Following the example of Boninsegni in Ref. [19], chosen form of the density matrix is:

$$\widehat{\rho}\left(\mathbf{R}_m, \mathbf{R}_{m+1}; \epsilon\right) = A_F\left(\mathbf{R}_m, \mathbf{R}_{m+1}; \epsilon\right) e^{-\epsilon U(\mathbf{R}_m)}. \tag{3.23}$$

Here, A_F is the exact density matrix of a system of N distinguishable, non-interacting particles, defined as:

$$A_F\left(\mathbf{R}_m, \mathbf{R}_{m+1}; \epsilon\right) = \Pi_{i=1}^N \widehat{\rho}_F\left(\mathbf{r}_{m,i}, \mathbf{r}_{m+1,i}; \epsilon\right), \tag{3.24}$$

where

$$\widehat{\rho}_F\left(\mathbf{r}_{m,i}, \mathbf{r}_{m+1,i}; \epsilon\right) = \left(4\pi\lambda\epsilon\right)^{-3/2} e^{-\frac{\left(\mathbf{r}_{m,i} - \mathbf{r}_{m+1,i}\right)^2}{4\lambda\epsilon}}. \tag{3.25}$$

In Eq. 3.23, function $U(\mathbf{R}_1)$ is defined by

$$U(\mathbf{R}_m) = \frac{2V(\mathbf{R}_m)}{3} + \tilde{V}(\mathbf{R}_m), \tag{3.26}$$

where $V(\mathbf{R}_m)$ is the total potential energy of a single time slice of configuration $\mathbf{R}_m$, same the one used in Eq. 3.22, and

$$\tilde{V}(\mathbf{R}_m) = \frac{2V(\mathbf{R}_m)}{3} + \frac{2\lambda\epsilon^2}{9} \sum_{i=1}^N \left(\nabla_i V(\mathbf{R}_m)\right)^2 \tag{3.27}$$

is valid if m is odd, and $\tilde{V}(\mathbf{R}_m) = 0$ if m is even. Here, the term $\nabla_i V(\mathbf{R}_m)$ is the gradient of the total potential energy of $\mathbf{R}_m$ configuration with respect to the coordinate $\mathbf{r}_{m,i}$ of i-th particle. This approximation is accurate to the order of ϵ^4 of the imaginary time power expansion of the density matrix in Eq. 3.18.

Using a fourth order approximation, it is possible to reduce the number of beads needed to achieve $\epsilon \to 0$ convergence up to the factor of 4 [20]. Further approximation schemes have been developed using factorization form for the exponential operator [21], but in this work, we will stick to Boninsegni's approximation.

3.2.2 Energy estimator

One of the basic physical quantities we can compute from a simulation is energy per particle, E/N. It can be obtained directly from a definition of energy of a canonical ensemble:

$$\frac{E}{N} = -\frac{1}{NZ} \frac{\partial E}{\partial \beta}, \tag{3.28}$$

where, as always, $\beta = 1/k_B T$. When we introduce PIMC terminology and permutation sampling, partition function Z of a bosonic system and finite temperature is

$$Z = \frac{1}{N!} \sum_{\mathcal{P}} \int \prod_{j=1}^{M} d\mathbf{R}_j \, (4\pi\lambda\epsilon)^{-\frac{3N}{2}} \, e^{-S(\mathbf{R}_j, \mathcal{P}\mathbf{R}_{j+1}; \epsilon)}. \tag{3.29}$$

Here, the periodic boundary condition for the imaginary time direction, $\mathbf{R}_{M+1} = \mathcal{P}\mathbf{R}_1$, still stands for different permutations $\mathcal{P}$ of particles, the system is specified as three-dimensional, hence the 3 in the $\frac{-3N}{2}$ exponent, and, as previously, $\lambda = \frac{\hbar^2}{2m}$ is used. We can directly evaluate the energy per particle using the predetermined action approximation, along with definitions Eq. 2.22, Eq. 2.24 and Eq. 2.25. What we get is the so called *thermodynamic estimator* [5] for total energy per particle:

$$\frac{E_T}{N} = \left\langle \frac{3}{2\epsilon} - \frac{1}{MN} \sum_{j=1}^{M} \frac{(\mathbf{R}_{j+1} - \mathbf{R}_j)^2}{4\lambda\epsilon^2} + \frac{1}{MN} \sum_{j=1}^{M} \frac{\partial U(\mathbf{R}_j, \mathbf{R}_{j+1}; \epsilon)}{\partial \epsilon} \right\rangle. \tag{3.30}$$

In a fashion similar to Eq. 3.28, it is possible to derive a thermodynamic expression for the kinetic energy per particle:

$$\frac{K}{N} = -\frac{m}{\beta Z} \frac{\partial Z}{\partial m}, \tag{3.31}$$

which, using the Eq. 3.29, also leads us to the thermodynamic estimator for kinetic energy:

$$\frac{K_T}{N} = \left\langle \frac{3}{2\epsilon} - \frac{1}{MN} \sum_{j=1}^{M} \frac{(\mathbf{R}_{j+1} - \mathbf{R}_j)^2}{4\lambda\epsilon^2} + \frac{m}{MN\epsilon} \sum_{j=1}^{M} \frac{\partial U(\mathbf{R}_j, \mathbf{R}_{j+1}; \epsilon)}{\partial m} \right\rangle. \tag{3.32}$$

The potential energy estimator can then be computed as a difference between Eq. 3.30 and Eq. 3.32, just like the inter-action in Eq. 2.25, and it is

$$\frac{V_T}{N} = \left\langle \frac{1}{MN} \sum_{j=1}^{M} \left(\frac{\partial U(\mathbf{R}_j, \mathbf{R}_{j+1}; \epsilon)}{\partial \epsilon} - \frac{m}{\epsilon} \frac{\partial U(\mathbf{R}_j, \mathbf{R}_{j+1}; \epsilon)}{\partial m} \right) \right\rangle. \tag{3.33}$$

In expressions Eq. 3.30, Eq. 3.32 and Eq. 3.33, the brackets $\langle ... \rangle$ mean the averaging over all sampled configurations. We can notice that the term $3/2\epsilon$ found in Eq. 3.30 and Eq. 3.32 is actually the energy of a classical ideal gas [5].

Unfortunately, the thermodynamic estimator for energy per particle in Eq. 3.30 has a distinct shortcoming regarding the computation if its statistical error. Since the first

two terms contain ϵ, they become larger as ϵ becomes smaller, so it gets harder to calculate a small difference between two large terms. For this reason, a new estimator was introduced, called the *virial estimator* [5]:

$$
\frac{E_V}{N} = \left\langle \frac{3}{2\epsilon} - \frac{1}{N} \sum_{j=1}^{M} \frac{(\mathbf{R}_{M+j} - \mathbf{R}_j)(\mathbf{R}_{M+j-1} - \mathbf{R}_{M+j})}{4\lambda\beta^2} \right.
$$
$$
+ \frac{1}{2\beta N} \sum_{j=1}^{M} (\mathbf{R}_j - \mathbf{R}_j^C) \frac{\partial}{\partial \mathbf{R}_j} \left[U(\mathbf{R}_j, \mathbf{R}_{j+1}; \epsilon) + U(\mathbf{R}_{j-1}, \mathbf{R}_j; \epsilon) \right]
$$
$$
\left. + \frac{1}{MN} \sum_{j=1}^{M} \frac{\partial U(\mathbf{R}_j, \mathbf{R}_{j+1}; \epsilon)}{\partial \epsilon} \right\rangle, \quad (3.34)
$$

where $\mathbf{R}_j^C = \sum_{l=1}^{M-1} (\mathbf{R}_{j+1} + \mathbf{R}_{j-l})/2M$. This estimator does not have the pathology of ever increasing terms with the reduction of imaginary time interval and makes the estimation of total energy per particle more precise and efficient than the thermodynamic estimator.

3.2.3 Superfluid density estimator

We already visited the topic of superfluid density in section 2.2.2. To measure this, one must take a closer look at moment of inertia of the system. Consider a liquid inside a container of cylindrical geometry, in thermal equilibrium with the walls of the container. We can measure the effective moment of inertia as the work done for infinitesimally small rotation of the walls [1, 22]:

$$
I = \left. \frac{\mathrm{d}F}{\mathrm{d}\omega^2} \right|_{\omega=0} = \left. \frac{\mathrm{d}\langle \widehat{L}_z \rangle}{\mathrm{d}\omega} \right|_{\omega=0}. \quad (3.35)
$$

Here, F is the free energy, and $\widehat{L}_z$ is total angular momentum operator of rotation around the axis of the cylindrical symmetry (designated as z), defined as the derivative by the cylindrical angle θ of all particles:

$$
\widehat{L}_z = i\hbar \sum_{i=1}^{N} \frac{\partial}{\partial \theta_i}. \quad (3.36)
$$

In contrast to this quantum definition, classical moment of inertia is a well known

$$
I_C = \left\langle \sum_{i=1}^{N} m_i (r_i^\perp)^2 \right\rangle, \quad (3.37)
$$

where $r_i^\perp$ is the cylindrical radial coordinate of i-th particle - a distance from the axis of rotation. Then, the ratio of quantum and classical moments of inertia is defined as

normal component density ρ_n of the liquid, and what remains is the superfluid density ρ_s, with $\rho = \rho_n + \rho_s$ being total density [1].

$$\frac{\rho_n}{\rho} = 1 - \frac{\rho_s}{\rho} = \frac{I}{I_C}. \tag{3.38}$$

However, since rotation is a motion of a system in real time, the definition of superfluid density in Eq. 3.38 is not so straightforward to implement within the PIMC algorithm scheme, built around the theory in imaginary time. Instead of observing the system with rotating walls, we can switch the inertial frame to one rotating with the walls. This makes the system a moving liquid with Hamiltonian $\widehat{H}_\omega = \widehat{H}_0 - \omega \widehat{L}_z$, where $\widehat{H}_0$ is the Hamiltonian of a liquid at rest [1, 22]. Starting from this, the so called *area estimator* for the superfluid density has been derived for a PIMC operating simulation [1, 23]:

$$\frac{\rho_s}{\rho} = \frac{2m \langle \mathbf{A}_z^2 \rangle}{\beta \lambda I_C}. \tag{3.39}$$

Here, the function $\mathbf{A}$ is the projected area of the paths, defined as

$$\mathbf{A} = \frac{1}{2} \sum_{i=1}^N \sum_{j=1}^M \mathbf{r}_{i.j} \times \mathbf{r}_{i,j+1}, \tag{3.40}$$

and its component along the rotation axis, $\mathbf{A}_z$, can be understood as a projection area of all polymers onto a plane perpendicular to the rotation axis [5]. Since the superfluid density is a diagonal observable, the estimator in Eq. 3.39 must be evaluated in a Z-sector configuration of closed polymers.

But, yet again, an implementation of an additional characteristic changes the definitions used. In a system with periodic boundary conditions, which is basically every computer simulation, cylindrical geometry is a naturally occurring feature, so it is simpler to calculate the superfluid density. Every system with periodic boundary conditions is topologically equivalent to a torus [6], so we will consider a liquid within two concentric cylinders with mean radius R and the spacing between the cylinders $d \ll R$. According to Eq. 3.39, the existence of a superfluid component requires a non-zero mean projected area of paths along the rotation axis [5]. This means that the only paths that will contribute to ρ_s are the ones winding around the torus, because all the others will have negligible effects when R is large enough. To this end, we define a *winding number estimator* [1] as

$$\frac{\rho_s}{\rho} = \frac{\langle \mathbf{W}^2 \rangle}{2\lambda \beta N}. \tag{3.41}$$

Here, $\mathbf{W}$ is the winding number, defined as the total flux of the paths winding around the torus, multiplied with circumference of the torus [5]. This definition is similar to the formula in Eq. 2.46, with the difference being that W in Eq. 3.41 is not an integer, but instead quantized as a multiple of the box length L. From a more general perspective, winding number can be calculated for any curve in a plane, and it represents total number

of times the curve travels counterclockwise around a point in the plane. In a system of polymers, the winding number can be calculated simply as

$$\mathbf{W} = \sum_{i=1}^{N} \sum_{j=1}^{M} \mathbf{r}_{i,j+1} - \mathbf{r}_{i,j}. \tag{3.42}$$

To gain more insight into the relation the between projected area and the winding number, let us take a closer look into the system between two cylinders, whose classical moment of inertia is $I_C = mNR^2$. If a path has wound around the periodic boundaries torus n times, then the area projection is n times the surface area perpendicular to the cylinder axis, $\mathbf{A} = R^2\pi n$. The flux of the path, or the winding number, is n times the circumference of the torus, $\mathbf{W} = 2R\pi n$. Therefore, the area is

$$\mathbf{A} = \frac{\mathbf{W}R}{2}, \tag{3.43}$$

which explains how Eq. 3.41 was obtained from Eq. 3.39. All this is illustrated by Fig. 3.11.
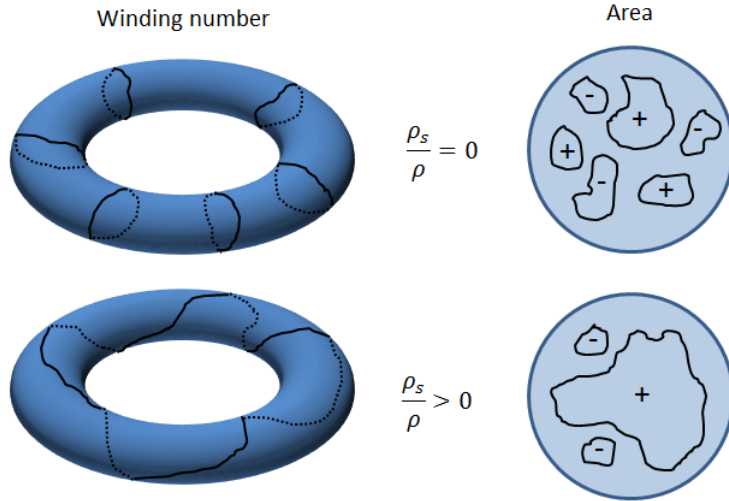

Figure 3.11: A comparison of calculation of superfluid density by using area estimator and winding number estimator. On the left side, a cylinder with periodic boundary conditions is shown mapped onto a torus. The right side shows projected area of paths in the axial direction. When the system shows no superfluidity (top), all the contributions of path projections cancel out and no path winds around the boundaries. When the superfluidity occurs (bottom), the net area projection and winding number, and therefore the calculated superfluid density, are non-zero. (Image modeled after a figure in Ref. [23].)

In the classical isomorphism, a system with non-zero superfluid fraction corresponds to the one with connected and/or intertwining polymers winding around the system boundaries, because in reality, particle exchange is necessary for superfluidity. To simulate this, updates involving roughly the order of $N^{1/3}$ particles are necessary [5], and PIMC single particle updates are not nearly enough to accomplish this. Fortunately, this is a problem also resolved by the worm algorithm sampling scheme, making it more efficient at calculating $\mathbf{W}$ reliably, and therefore the superfluid component density as well.

3.3 The Code

Writing a computer program that would include all of the so-far listed features in a methodical, understandable and user-friendly way is a major undertaking that requires a lot of time and effort. We are grateful to M. Boninsegni for providing us with the functional written code, which will be described in this section.

The program itself is written in C++ language and completely object-oriented. The code covers a wide variety of physical systems and circumstances, so user is almost completely devoid of having to meddle with the source code for additional functionality. It contains a custom-build script lexer, which obliges the user to adjust the input files and parameters just by writing external scripts that the program reads and processes. Also, it comes with the well suited functionality for usage on clusters and other Linux-based operating systems.

The only part of the code user must modify is the calculation of the potential. Since the potential is a characteristic of every different physical system, it is hardly possible to construct a general way of implementing it within the code. Still, with this program being passed around the scientific community, it already comes with many unique potentials to choose from, and only requires a basic knowledge in C++ to create your own. For the algorithm itself, the potential input can be realized in three different ways:

- Point potential - this is a spherically central potential dependent of the distance between two points.

- Line potential - a cylindrically central potential that depends on a distance from a line.

- Plane potential - a potential that depends on the distance from a plane.

The user can input as many potentials as desired. To use line or plane potentials, lines and planes must be instanced as separate objects; this is all controlled with the input scripts. Once all the potentials are calculated, the grid containing the interaction data is created. This way to implement the potential within a simulation is somewhat restricted and may be seen as a weak point of the code.

An example of the input script that must be supplied by the used is given in Tab. 3.1. When the simulation is over, many output files are provided, containing various statistics, estimators, calculated potentials and other data, specific to particle types or otherwise.

BOX $\langle \#dimensions \rangle$ $\left\langle \begin{array}{c} x\,box \\ size \end{array} \right\rangle$ $\left\langle \begin{array}{c} y\,box \\ size \end{array} \right\rangle$ $\left\langle \begin{array}{c} z\,box \\ size \end{array} \right\rangle$

TYPE $\langle name \rangle$ $\langle symmetry \rangle$ $\left\langle \frac{\hbar^2}{2m} \right\rangle$ $\langle \#particles \rangle$ $\left\langle \begin{array}{c} input \\ file\,name \end{array} \right\rangle$

LINE $\langle name \rangle$ $\langle spatial\,direction \rangle$ $\left\langle \begin{array}{c} other \\ coordinate\,1 \end{array} \right\rangle$ $\left\langle \begin{array}{c} other \\ coordinate\,2 \end{array} \right\rangle$

POTL $\left\langle \begin{array}{c} type \\ name\,1 \end{array} \right\rangle$ $\left\langle \begin{array}{c} type \\ name\,2 \end{array} \right\rangle$ $\left\langle \begin{array}{c} potential \\ number \end{array} \right\rangle$ $\left\langle \begin{array}{c} lower \\ cutoff \end{array} \right\rangle$ $\left\langle \begin{array}{c} upper \\ cutoff \end{array} \right\rangle$ $\left\langle \begin{array}{c} grid \\ points \end{array} \right\rangle$ $\left[\begin{array}{c} additional \\ parameters \end{array} \right]$

TEMP $\langle temperature \rangle$ `//in Kelvins`

RESTART   `(?)` `//if restarting`

SLICES $\langle \#time\,slices \rangle$

PASS $\langle \#blocks \rangle$ $\langle \#steps \rangle$

AREA $\left\langle \begin{array}{c} type \\ name \end{array} \right\rangle$ $\left\langle \begin{array}{c} projection \\ coordinate \end{array} \right\rangle$ $\langle cutoff \rangle$ $\left\langle \begin{array}{c} grid \\ points \end{array} \right\rangle$

IMD $\left\langle \begin{array}{c} type \\ name \end{array} \right\rangle$ $\left\langle \begin{array}{c} Ira-Masha \\ distance \end{array} \right\rangle$ `//in beads`

GSECTOR/ZSECTOR `(?)` `//if simulating either` `Z`-`sector or` `G`-`sector configuration`

Table 3.1: A sample input script for the program. All values that the used is required to input are marked by $\langle ... \rangle$ parenthesis. Values with a `(?)` are optional. This particular input script simulates a single type of particles interacting with a line via cylindrically-symmetric potential. The user can add as much TYPE arguments for different particle types, LINE arguments for definition of different lines and POTL arguments for different interactions.

4 Simulations

The focus of this chapter will be actual results from the conducted simulations, putting into use everything discussed in two previous chapters. We will start with the full and thorough description of a system of helium atoms in a cylinder, along with all the quantities and measures. For nanopores without disorder, results from the Ref. [3] will be presented. Then, the same will be done for the system with impurities on the walls of the pore, starting with the changes in the system settings and potential, and some known and relevant physical quantities as a test for the algorithm. Finally, we will review results for the superfluid density fraction with the disorder included.

4.1 Helium in a nanopore

Lets start with the description of the model of ^{4}He in a cylindrical cavity. This system is described by the Hamiltonian

$$\widehat{H} = -\frac{\hbar^2}{2m} \sum_{i=1}^{N} \nabla_i^2 + \sum_{i=1}^{N} V(r_i) + \sum_{i<j}^{N} U(r_{ij}), \tag{4.1}$$

where N is the number of atoms of mass m, $V(r)$ is the external confining potential acting on them, and $U(r_{ij})$ is their interaction potential at a distance between two atoms r_{ij}.

Experimental results show helium is highly attracted to the walls of the pore. Initially, when ^{4}He is introduced into the porous media, some of the liquid is deposited onto the walls. Neutron scattering shows that these layers are comprised of amorphous solid helium about 5 Å thick. As for the rest of ^{4}He, it is contained as a liquid inside those solid layers confined by the walls of the nanopore. The walls of solid helium are inert, while the liquid inside can sustain superflow and BEC [3]. This is all illustrated in Fig. 4.1.

To reduce the computational demands, we are simulating only the liquid on the inside of inert helium layers of the pore, since only that part of the system gives rise to the relevant physical phenomena, such as the superflow. Still, solid ^{4}He walls play an important role in the potential that particles on the inside feel. This is relevant for the way the pore itself is implemented into the simulation. Regardless of the outside media, the only computational property that simulates the presence of the pore is the confining potential.
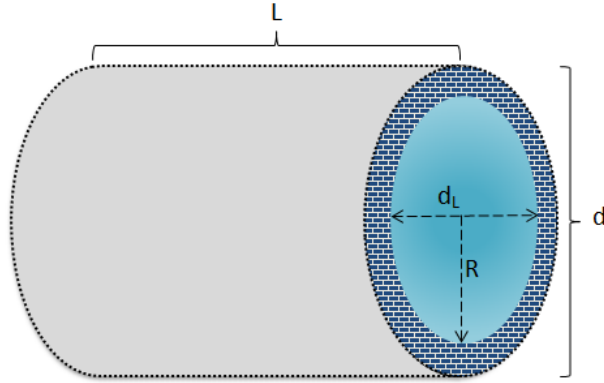
Figure 4.1: A schematic representation of ^{4}He system inside a nanopore. The mottled
area represents inert walls of solid helium of $5 - 6\,\text{Å}$ thickness. The lightblue
area represents the rest of the system as a confined liquid that can sustain
superflow and BEC. L is the length of the entire pore, R is the radius and
d_L the diameter of a cylinder occupied by the liquid fraction of the system,
so that the diameter of the whole nanopore is $d = d_L + 10\,\text{Å}$.

It has the form of

$$
V(r) = 3\epsilon n \pi \sigma^6 \int_R^{R_i} r_s \mathrm{dr_s} \int_0^\pi \mathrm{d}\phi_s
$$
$$
\left[\frac{21}{32} \frac{\sigma^6}{(r^2 + r_s^2 - 2rr_s \cos\phi_s)^{11/2}} - \frac{1}{(r^2 + r_s^2 - 2rr_s \cos\phi_s)^{5/2}} \right]. \quad (4.2)
$$

It consists of double integration by polar coordinates r_s and ϕ_s of Lennard-Jones (L-
J) pair potential between ^{4}He and medium atoms. Here, the medium begins at the
pore radius R and ends at radius chosen to be $R_i = 3R$. It is comprised of concentric
cylindrical surfaces of infinite length, and incorporates both the inert helium walls and
standard pore atoms. Potential parameters have been set so that the system on the inside
of the pore remains liquid: Lennard-Jones parameters $\sigma = 2.2\,\text{Å}$, $\epsilon = 3\,\text{K}$, and number
density of the medium $\rho_{med} = 0.078\,\text{Å}^{-3}$ [3]. The resulting potential is homogenous in
both the polar angle and along the axis of the pore, so it only depends on the distance
from the axis, r. One such dependance is shown in Fig. 4.2. A cylindrically symmetric
potential defined this way is ideally implemented with the POTL argument mentioned
in Tab. 3.1.

As for the ^{4}He atoms themselves, they interact with each other via Aziz interatomic
potential [3, 24]. It is a very realistic representation of the potential between helium atoms
proven to reliably simulate many size sensitive properties, with a total of 14 parameters
to be tailored for the needs of a specific system being simulated. More on the details and
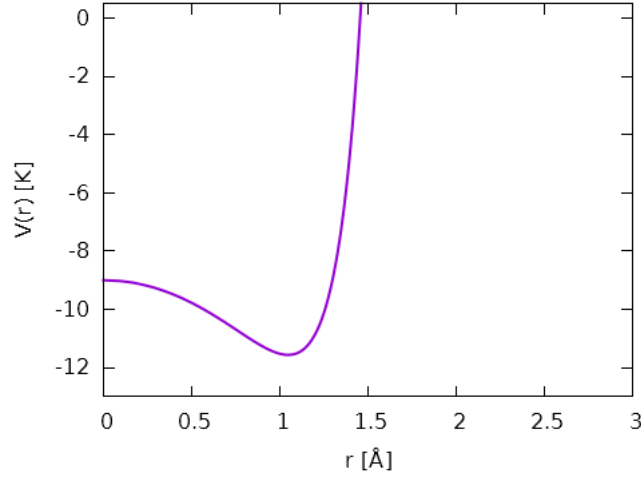the coefficient values for ^{4}He can be found in Ref. [24].

Figure 4.2: A cylindrical cavity potential profile, shown for the pore of $R = 3\,\text{Å}$. It is homogenous in both ϕ and z polar coordinates, so this curve is the same, seen from any angle and on any height. The shallow attractive medium followed by a strong repulsive rise are enough to incorporate the presence of a nanopore of inert helium walls and some outside media into simulation.

To summarize, we are running a series of PIMC simulations of low temperature[6] ^{4}He atoms interacting with the Aziz potential, confined inside a cylindrical cavity of solid helium layers and some porous media, represented by the potential in Eq. 4.2. Radius of this pore is chosen to be $R = 3\,\text{Å}$ always, or in other words, it is a very narrow nanopore. Reasons for this will be discussed in the following section.

4.1.1 Known results

As mentioned previously, an extensive study in Ref. [3] has been conducted, aimed at low energy properties of bosonic helium systems in porous media. It included calculation of one-body density matrix and superfluid density. The purpose of this research was to gain a better insight into scarcely explored world of systems in pores, particularly because they seem to scale as vastly different models, depending on physical circumstances.

One property we highlight in this thesis is superfluid density. Depending on the radius of nanopores, superfluid properties seems to scale according to the models of different dimensions, as shown in Fig. 4.3. At pore radius of $R \geq 11\,\text{Å}$, there are indications of both 3D and 2D fluid scaling, depending on both the temperature T and the pore length L and approaching bulk 3D liquid. For the radius interval $4\,\text{Å} \leq R \leq 11\,\text{Å}$, the liquid scaling is predominantly 2D. In this regime, oscillations in radial density profiles indicate that the liquid fills the pore in cylindrical layers, unlike the 3D scaling case, where the oscillations are suppressed and radial density is overall smoother [3].

---

[6]Simulations will differ by parameters such as number of particles, temperature etc. More on that topic later on.
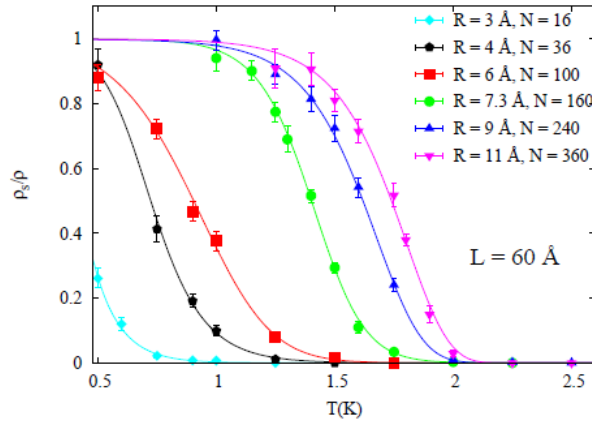
Figure 4.3: Different scaling of the superfluid fraction ρ_s/ρ as function of temperature T, depending on radius of the pore R, at pore length $L = 60\,\text{Å}$. Scaling ranges from nearly 3D bulk liquid at $R = 11\,\text{Å}$, through 2D liquid deposited in film-like layers, to 1D Luttinger liquid model at $R = 3\,\text{Å}$. In other words, the scaling dimension of a ^{4}He system in a nanopore increases with the increase of pore radius. (Image taken from Ref. [3])

Finally, one-dimensional scaling of the superfluid fraction is consistent with the predictions of Luttinger liquid theory, and Eq. 2.49. The system falls into this regime in only the narrowest nanopores simulated, with $R = 3\,\text{Å}$. The small radius seems to play an important role in 1D nature of this scaling. In a narrow nanopore, the potential minimum in Fig. 4.2 is not attractive enough to force the particles to spread much from the cylindrical axis, where the liquid density is at its maximum. Also, dimensions of the pore are simply too small to enable free motion in any direction other than along the axis. This makes the bosons that are simulated effectively fermions, without actually imposing Fermi-Dirac statistics to their exchange cycles, which may account for LL scaling because that model is generally valid for fermions. Of course, all of these conclusions are made with respect to the hard core diameter of ^{4}He atoms of $d_{HC} \simeq 2.5\,\text{Å}$ [3].

As an extension of this study, we are interested in superfluid properties in the 1D, Luttinger liquid scaling regime. So, the nanopores chosen for simulations have all been set to $R = 3\,\text{Å}$. As for the box, it is a 3D square with ^{4}He atoms positioned around the origin of the cylindrical cavity potential in Eq. 4.2 and periodic boundary conditions in all directions. Of course, the boundary conditions are only expected to be invoked in direction of the cylindrical axis, since the potential prevents the atoms from ever exiting the pore area.

4.2 Adding the disorder

So far, we have only discussed nanopores with a smooth, completely homogenous potential confining the particles inside. In a realistic scenario, even a nanopore without any other added source of interaction is an example of disordered potential. Because of, among other reasons, inner surface deformities and varying thickness of inert helium walls[7], the potential can appear irregular. This disorder can greatly affect superfluid properties, as it has been shown that adding disorder in form of some external potential suppresses the superfluid fraction [3].

This work extends the study of disorder effects on superfluidity, in a literal sense. Additional disorder potential will originate from atoms of impurities scattered around the walls in the virtue presented in Ref. [3]. These impurities are fixed in place, which is achieved in simulation by making their mass infinite with $\lambda_{dis} = 0$. They do not interact with each other, and interact with ^{4}He atoms on the inside with a simple Lennard-Jones potential. Then the Hamiltonian of the inside system still has the form of Eq. 4.1, with just the addition of this static L-J interaction into external potential. The parameters are set to $\sigma_{dis} = 2\,\mathring{A}$ and $\epsilon_{dis} = 1.5\,K$, which accounts for a fairly weak interaction. Other, much stronger interactions have already been shown to drastically suppress the superfluid fraction [3].

Regarding the placement of these atoms, they are spread around the nanopore very close to the surface. For every simulation, mean linear density along the pore axis is kept at $\Lambda_{dis} = 1\,\mathring{A}^{-1}$. To avoid clustering the impurities into pockets of strongly interacting inhomogeneities, their positioning is generally preferable not to be completely random, although this option is not intentionally avoided. Firstly, since every pore has $R = 3\,\mathring{A}$, the radial coordinate is taken randomly from the interval $r_{dis} \in [2.5, 3.5]\,\mathring{A}$, and the polar angle is chosen randomly from $\phi_{dis} \in [0, 2\pi]$. As for their height, there are several possible models of placement. We used two approaches - one completely random, from the interval $z_{dis} \in [0, L]$, and one with the disorder duplicated from pores of smaller L, copied multiple times if needed to fill the entire length, and with respect to mean linear density. We found that, for a pore of $L = 30\,\mathring{A}$ and $N = 4$, results show no significant difference in either case. We emphasize this is not a dismissible matter and further study is viable for different models of disorder, but that was not the focus of our study. The chosen model is random placement of disorder along the $z-$axis.

One thing to note here is that, even though impurities are placed according to some rules, their presence is still meant to be random by nature. We did not introduce the disorder in any systematic was or used any measure of classification for it. There have been attempts to classify the disorder and the effects it produces in other studies, such as Ref. [4], but that is not a focus of this study. We used disorder with the intent to be just that - a disordered, irregular and relatively random source of outside potential. An experimental study, for instance, would likely require many different realizations of this example.

The addition of impurities distorts the potential that atoms inside of the pore feel. The

---

[7]Thickness of $5-6\,\mathring{A}$ translates to $1-1.5$ layers of ^{4}He wall atoms [3].

randomness of their placement effectively breaks all homogenous properties of previously described potential of a smooth pore in Eq. 4.2, as intended. This is shown in Fig. 4.4. Note that the attractive minima and the repulsive centers of the potential have been shifted in both position and value from profile presented in Fig. 4.2. The effects of these modifications on physical properties will be presented in the next two sections.

4.2.1 Preliminary results

At this point, we are able to examine the results of our simulations to develop some intuition about what kind of a system we are dealing with. Firstly we will focus on different realizations of the disorder. Altought, as mentioned in the previous section, we do not classify the disorder in any way, it would be senseless to assume that differences in disorder do not produce different results. Still, we are operating under an assumption that these differences are not significant enough to become a prevalent issue.

The differences in impurity configurations arise from random nature of their positioning. Every pseudorandom number generator works by algebraically manipulating *seeds* - numbers or sets of numbers given as initial values. We have tested the properties of our system for disorder configurations generated from five different seeds. Keep in mind that their actual values are unimportant and that results would qualitatively be the same for any other values, handpicked or generated in any other way. This test of the algorithm was done for pores of $L = 30 \, \text{Å}$ length with $N = 4$ atoms and at temperature $T = 1 \, \text{K}$.

Lets start with the results for energy per particle E/N and superfluid fraction ρ_s/ρ for different disorders. Histograms of these quantities are shown in Fig. 4.5. Results display similar behavior for both quantities - minor offsets of some mean well within error bars. The conclusion we can draw from this is that E/N and ρ_s/ρ are not very sensitive to differences in disorder realizations, at chosen values of physical parameters. Still, it is obvious that the superfluid fraction displays more variation than energy per particle. Although these variations are in the regime of small values $\rho_s/\rho < 0.02$ of suppressed superflow, it is something so acknowledge for further results and discussions. This implies that superfluid properties are more influenced by fine size local effects that the disorder brings into the potential, which is not expected from an intensive property like E/N.

Next things we explore are correlations and density. The *pair-correlation function* $g(\mathbf{r}_1, \mathbf{r}_2)$ is a measure of density variations from a reference particle. It is defined as probability to find a particle at $\mathbf{r}_2$ when another particle is at $\mathbf{r}_1$. In a uniform system, like ^{4}He atoms in a nanopore, it only depends on a distance between two particles $r = |\mathbf{r}_2 - \mathbf{r}_1|$ [5]. Also known as *radial distribution function* (RDF), $g(r)$ is used to describe the microscopic arrangement of particles in a system. It has a characteristic shape for different phases of matter, which is highly insensitive to differences in quantum and classical nature of particles, and valid for Bose and Boltzmann statistics with minimal offsets [1]. It is preferable to study $g(z)$, where z is the polar coordinate, in a 1D model where the system is expected to be distributed along the $z-$axis, but the simulation
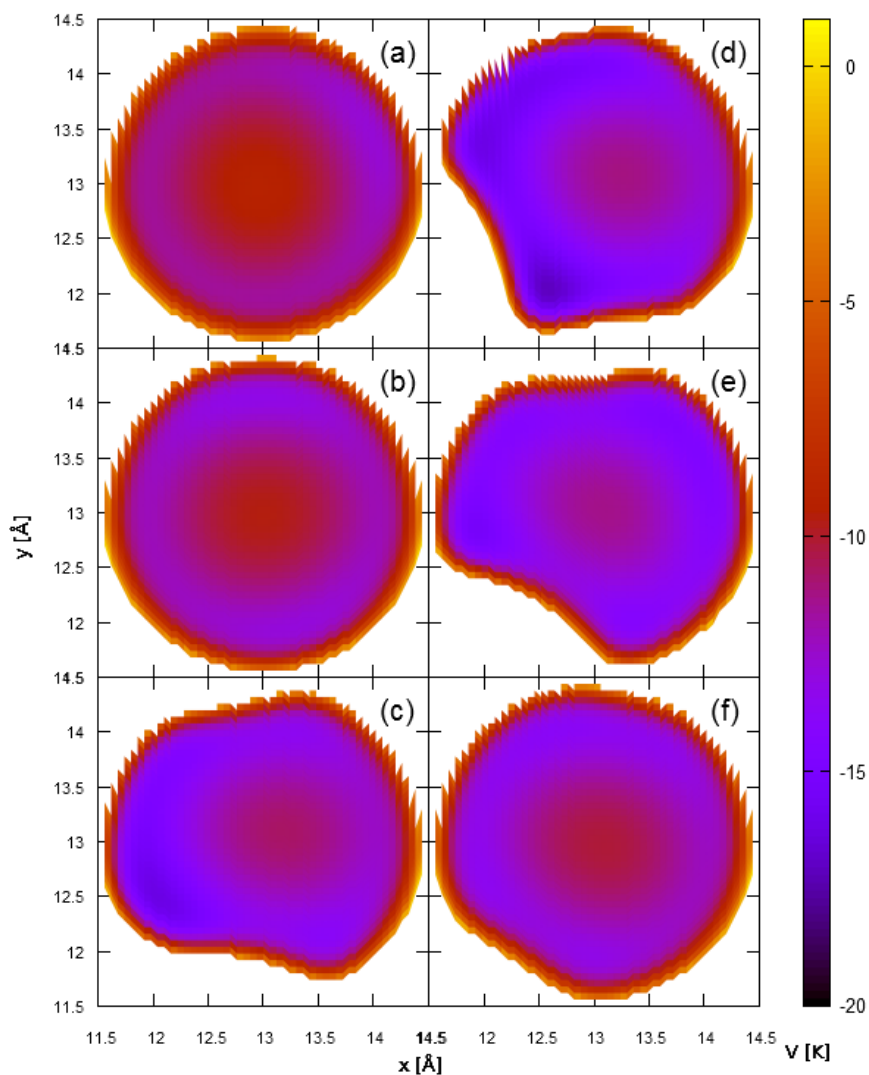
Figure 4.4: Potential profiles for a nanopore of $L = 30\,\text{Å}$ centered at $x_c = y_c = 13\,\text{Å}$, and with $N_{dis} = 30$ atoms of disorder, in dependance of x and y coordinate. Profiles are shown at heights of (a) $z = 0\,\text{Å}$, (b) $z = 6\,\text{Å}$, (c) $z = 10\,\text{Å}$, (d) $z = 14\,\text{Å}$, (e) $z = 21\,\text{Å}$ and (f) $z = z = 28\,\text{Å}$. Upper cutoff of $1\,\text{K}$ was used. Distorted shapes of these profiles originate from zones of strong repulsion created by atoms of impurities around the surface.

algorithm supplied us with the 3D $g(r)$. We introduce a normalization

$$g_{1D}(r) = g(r)\frac{3r^2}{(L/2)^2}, \tag{4.3}$$

which is an artificial way to rescale the behavior of RDF into one-dimensional regime.

Results are shown in Fig. 4.6a. All simulation results show a well known RDF profile of a liquid system. For 1D systems, pair-correlation function derived from the LL theory contains oscillatory terms that are more pronounced for higher densities and harder to detect for smaller L [14]. Our results show no oscillations, as expected from a liquid of given density, although one of the RDF-s, colored blue in Fig. 4.6a, stands out with slightly pronounced variations. Fig. 4.6b also shows a radial density profile for same systems. The results practically overlap completely, as expected from a 1D scaling liquid of given density [3]. This means that the liquid is confined to the center of the nanopore in all cases of disorder.
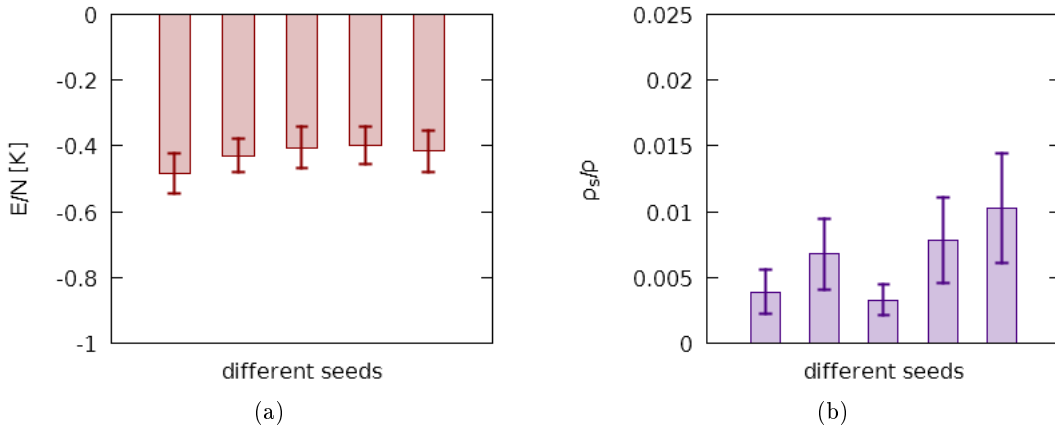
Figure 4.5: Results of 5 simulations using different configurations of disorder of (a) energy per particle E/N, and (b) superfluid fraction ρ_s/ρ, for a nanopore of $L = 30\,\text{Å}$, $N = 4$ and $T = 1\,\text{K}$. The dependance are not functional in either case so horizontal axes have no physical meaning.

Lastly, we present a preliminary result of a temperature dependance of superfluid fraction ρ_s/ρ, before moving on to different dependance of this quantity. Results are calculated for different numbers of particles in a pore of $L = 30\,\text{Å}$; that is, for different linear densities $\Lambda = N/L$. This is shown in Fig. 4.7. Looking at these results, one might draw a conclusion that the superfluid fraction is higher for higher linear densities and drops as the temperature increases. While this is correct for this particular case, the system is not expected to scale with T only. As pointed out in Sec. 2.2.2, Luttinger liquid scales with LT product, and not independently, so the dependance on just temperature does not fall under the properties of the model we are studying. Further results for the superfluid density in LL scaling regime will be given in the next section.

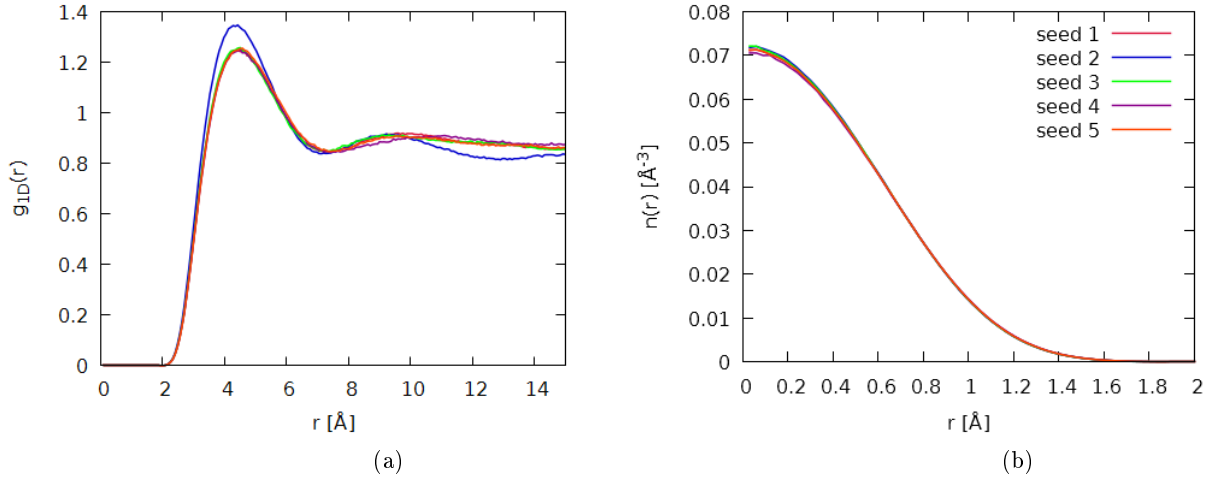(a)   (b)

Figure 4.6: Results for 5 simulations with different configurations of disorder originating from different seeds of a random number generator, of (a) pair-correlation function $g_{1D}(r)$ and (b) radial density profile $n(r)$ for a nanopore of $L = 30$ Å, $N = 4$ and at $T = 1$ K. All results overlap, displaying almost identical profiles, except a slight variation from one of RDF-s, colored blue. This curve still describes a liquid, though, with higher density of first neighbors.
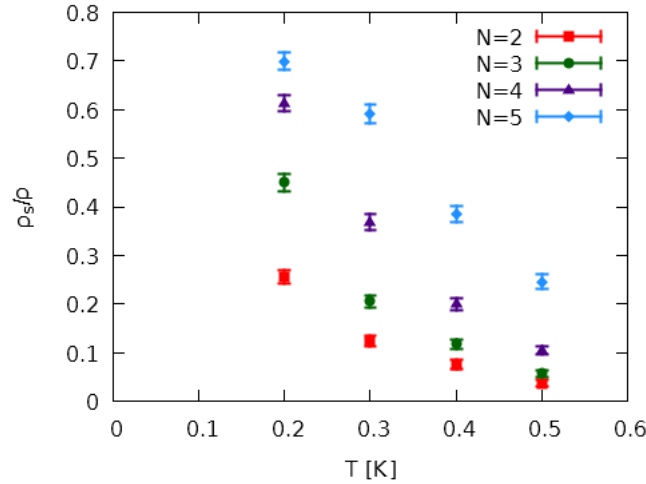
Figure 4.7: Superfluid fraction ρ_s/ρ in dependence of temperature T, for a nanopore of $L = 30$ Å and with $N = 2, 3, 4, 5$ atoms. Corresponding linear densities are $\Lambda = 0.067, 0.1, 0.133, 0.167$ Å^{-1} respectively. Results indicate a drop in superfluid density with the increase of temperature and a rise with the increase of density.

4.2.2 Superfluid density

We have discussed the topic of superfluidity on several occasions already, in Secs. 2.2.2 and 3.2.3, and had our goals set to exploration of scaling of superfluid fraction in the low energy region, for the system of helium atoms in disordered and narrow nanopores. Since previously known results [3] indicate that this system behaves as a one-dimensional fermion liquid, superfluid fraction is expected to scale according to Luttinger liquid predictions, in the virtue of Eq. 2.49. The Tomonaga-Luttinger model is an effective theory, valid for virtually any potential, including systems with disorder, so the presence of impurity atoms should not be an exception for this.

Superfluid properties are closely tied to the phase factor of density field [6, 13]. This influence is controlled by the Luttinger parameter v_J, as displayed in Eq. 2.42 Hamiltonian. A harmonic 1D liquid of spinless fermions, like an LL model system, is expected to scale with a single variable $x = L/(\hbar\beta v_J)$ [3], that incorporates both LT dependance and LL parameter v_J. The parameter is expected to be universal - insensitive to thermodynamic variables and finite-size effects, for a given model.

This has been confirmed for homogenous nanopores in Ref. [3] with a good fit. In this case, density of the liquid helium in the inner layer of the pore was kept close to the density of bulk liquid helium at saturated vapor pressure (SVP). The results were fit to Eq. 2.49 with $\hbar v_J$ as a free parameter. Good agreement was shown with Eq. 2.43, thus confirming the LL model for uniform nanopores.

In this work, we are interested in comparison of superfluid fraction results for disordered nanopores with the results for uniform ones. We refer to the results derived by Prokof'ev and Svistunov in Ref. [25], which shows that in 1D, starting from two different ways of defining the superfluid density one gets different expressions, unlike the situation in 3D. In PIMC, a *thermodynamic* superfluid fraction has been derived as a response to the flux gauge field, defined by the change in Helmholtz free energy by the superfluid velocity: $\rho_s/\rho = \partial(F_v/N)/\partial(\frac{1}{2}mv^2)$ [14, 12]. This definition is used to obtain Eq. 2.49. On the other hand, Prokof'ev and Svistunov define a *dynamical* superfluid density ρ_s^D as a coefficient in effective long-wavelength action $F_{eff} = (\rho_s^D/2)\int dV(\nabla\Phi)^2$ of a liquid which includes twists of phase Φ [25]. In 1D, the two expressions are different. Thus, using general relation in Eq. 2.48 a reformulation of Eq. 2.49 is introduced:

$$\frac{\rho_s}{\rho} = \frac{\pi LT}{4\hbar v_J^0} \frac{\left|\vartheta_3''\left(0, e^{-\pi LT/2\hbar v_J^D}\right)\right|}{\vartheta_3\left(0, e^{-\pi LT/2\hbar v_J^D}\right)}. \tag{4.4}$$

Here, v_J^0 is a constant for a given density, defined by Eq. 2.43 and valid in case of uniform nanopores. Parameter v_J^D is then defined as

$$v_J^D = \frac{\rho_s^D}{\rho}v_J^0. \tag{4.5}$$

Eq. 4.4 provides a relation between ρ_s/ρ and ρ_s^D/ρ. In a uniform nanopore, predictions of LL theory are valid, therefore $\rho_s^D/\rho = 1$, so that a constant $v_J^D = v_J^0$ defines Eq. 2.49.

If they are not valid in disorder, the coefficient ρ_s^D/ρ can be used as a fitting parameter for Eq. 4.4. Hence, this coefficient contains the differences in 1D results arising from two definitions of superfluid fraction [14].

For a disordered nanopore, we use $x = L/(\hbar\beta v_J^0)$ as a scaling variable for results. Unlike Ref. [3], the density of systems we studied is not kept at bulk density at SVP - we show results grouped by five different linear densities. The results were fit to Eq. 4.4 using ρ_s^D/ρ as a free fitting parameter. This is shown in Tab. 4.1, and Figs. 4.8, 4.9, 4.10, 4.11 and 4.12.

$\Lambda\,[\mathring{A}^{-1}]$	ρ_s^D/ρ	$\hbar v_J^0\,[K\mathring{A}]$	$\hbar v_J^D\,[K\mathring{A}]$	χ^2
0.067	0.82018 ± 0.04879	2.55257	2.09357	27.4373
0.100	0.86565 ± 0.02283	3.80981	3.29796	37.3829
0.133	0.77213 ± 0.01602	5.06705	3.91242	18.6521
0.200	0.97524 ± 0.00829	7.61962	7.43096	21.3907
0.250	0.88489 ± 0.02430	9.52452	8.42812	47.4002

Table 4.1: Values of a fitting parameter ρ_s^D/ρ, constant thermodynamic Luttinger parameter $\hbar v_J^0$, dynamical Luttinger parameter $\hbar v_J^D$, and χ^2 values of fits, for different linear densities of Λ of helium atoms.
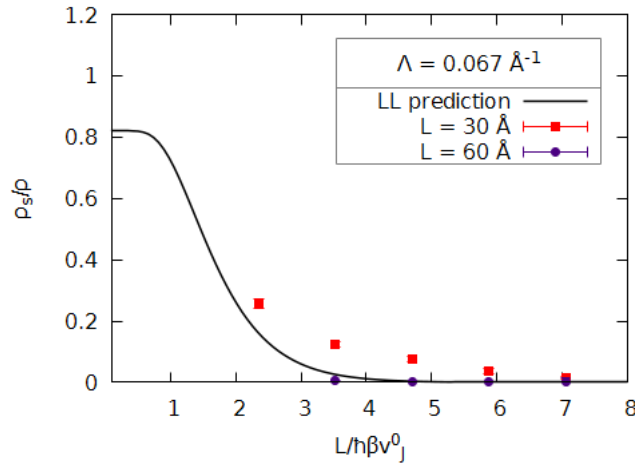

Figure 4.8: Superfluid fraction ρ_s/ρ in dependance of the scaling variable $L/(\hbar\beta v_J^0)$ for linear density of $\Lambda = 0.067\,\mathring{A}^{-1}$ and different pore lengths and temperatures. The results fit with a parameter value of $\rho_s^D/\rho = 0.82$.

Conclusion we can draw from the presented figures are ambiguous at best. Starting from the lowest density $\Lambda = 0.067\,\mathring{A}^{-1}$ seen in Fig. 4.8, it is obvious that the results are barely in contact with the fitting curve and the scaling is completely broken. Similar case occurs at the highest density $\Lambda = 0.25\,\mathring{A}^{-1}$ shown in Fig. 4.12. Densities of $\Lambda = 0.1\,\mathring{A}^{-1}$

and $\Lambda = 0.133\,\text{Å}^{-1}$ show similar behaviors, as seen in Figs. 4.9 and 4.10 respectively, although with more points closer to the fits.
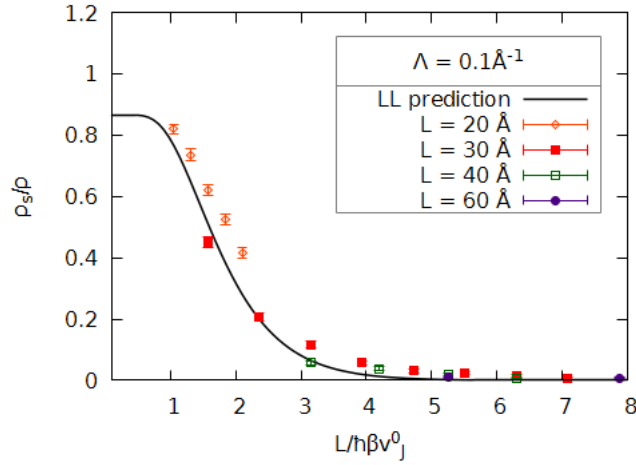

Figure 4.9: Superfluid fraction ρ_s/ρ in dependance of the scaling variable $L/(\hbar\beta v_J^0)$ for linear density of $\Lambda = 0.100\,\text{Å}^{-1}$ and different pore lengths and temperatures. The results fit with a parameter value of $\rho_s^D/\rho = 0.87$.
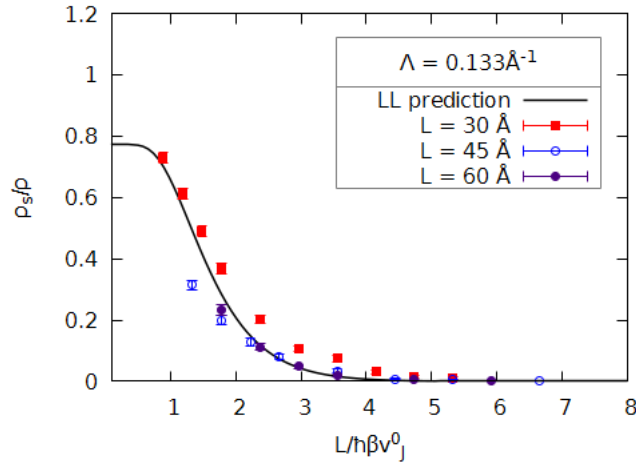

Figure 4.10: Superfluid fraction ρ_s/ρ in dependance of the scaling variable $L/(\hbar\beta v_J^0)$ for linear density of $\Lambda = 0.133\,\text{Å}^{-1}$ and different pore lengths and temperatures. The results fit with a parameter value of $\rho_s^D/\rho = 0.77$.

Loosely speaking, the "best" scaling is seen for $\Lambda = 0.2\,\text{Å}^{-1}$ in Fig. 4.11, in a sense that the parameter ρ_s^D/ρ is closest to 1, and thus closest to the case of uniform nanopores that confirm the LL model. Still, even though some data fits the expected curves well,

the LL parameters v_J^D is different from the theoretical prediction of v_J^0 in Eq. 2.43 for every case. The values of fitting parameters and χ^2 are listed in Tab. 4.1. Given the expected universality of LL parameters and very high χ^2 values for each fit, the only conclusion left to make out of these results is that a system of helium atom in a narrow disordered nanopore does not in fact scale with the LL theory of 1D fermions. Reasons for this will be discussed in the next chapter.
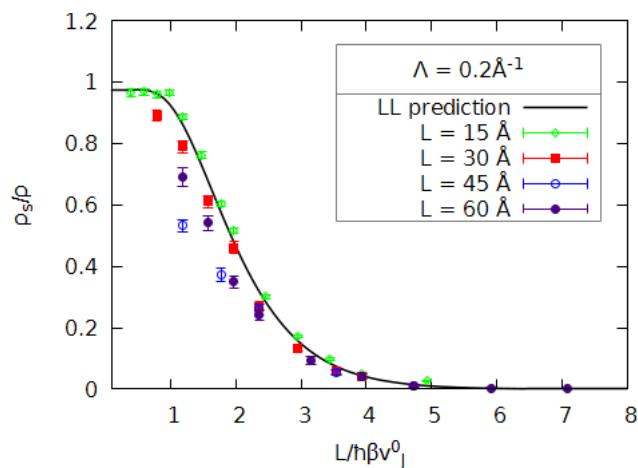

Figure 4.11: Superfluid fraction ρ_s/ρ in dependance of the scaling variable $L/(\hbar\beta v_J^0)$ for linear density of $\Lambda = 0.200\,\text{Å}^{-1}$ and different pore lengths and temperatures. The results fit with a parameter value of $\rho_s^D/\rho = 0.98$.
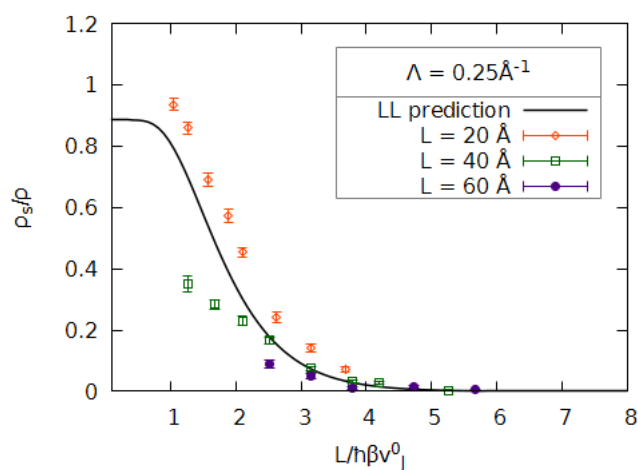

Figure 4.12: Superfluid fraction ρ_s/ρ in dependance of the scaling variable $L/(\hbar\beta v_J^0)$ for linear density of $\Lambda = 0.25\,\text{Å}^{-1}$ and different pore lengths and temperatures. The results fit with a parameter value of $\rho_s^D/\rho = 0.88$.

5 Discussion

Considering the universality of Luttinger parameters and good agreement of results and theory in the case of homogenous nanopores, we expected the results of nanopores with disorder to fit well, and within error bars of fitting parameters, with the predictions of LL model. This assumption has been further supported by the fact that different realizations of disorder seem to have only marginal influence on energy and superflow properties in Fig. 4.5, and, for all instances of disorder, the system was identified as a liquid confined to central axis of the nanopore by structural properties in Fig. 4.6. Instead, our data shows a large disparity of fitting parameters, as seen in Tab. 4.1, and overall poor agreement with the fit curves.

All of the curves that fit the data to Eq. 2.49 for used linear densities are displayed in Fig. 5.1. If our expectations for the results had proved correct, all of the shown curves
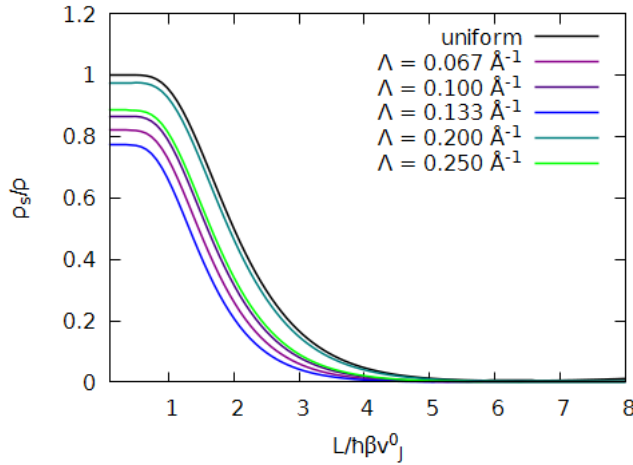

Figure 5.1: Superfluid fraction ρ_s/ρ curves in dependance of $L/\hbar\beta v_J^0$ variable, for different linear densities we simulated. The fitting parameters are listed in Tab. 4.1 and they all differ from the fit of smooth nanopore data.

would have the same profile with minimal differences and distances from one another. This is obviously not the case, which demands an explanation.

Firstly, let us consider one crucial aspect of the LL model - the one-dimensionality. The main reason for 1D scaling is the narrowness of the nanopores; at $R = 3\,\mathring{A}$, ^{4}He atoms of $d_{HC} \simeq 2.5\,\mathring{A}$ practically have only one degree of freedom, which is motion along the pore axis. In addition, homogenous nature of the confining potential in the case of uniform nanopores also accounts for the 1D scaling. While the latter is obviously

not the case for disordered pores, as discussed and shown in Fig. 4.4, the former is even more so valid. In other words, even though there are differences in potential along the z-axis and the polar angle, the repulsive interactions with impurity atoms suppress the radial and angular degrees of freedom of helium atoms even further, contributing to their confinement inside the pore and emphasizing the 1D scaling regime. This *quasi*-1D nature is still not expected to break the scaling of the LL model.

For the density of $\Lambda = 0.067\,\text{Å}^{-1}$, the disagreement with the model is actually quite straightforward to explain. At this density, the system is below the point of spinodal decomposition. This unstable thermodynamic state occurs inside the inflection curve of Gibbs free energy in phase diagram, where its second derivative by density equals zero. It is characterized by local to macroscopic separation of phases of a homogenous system into a non-homogenous one [26]. For a uniform system like ours, sub-spinodal state includes formation of liquid droplets and reduction of sound velocity to zero. In the case of homogeneous pore, spinodal density is $\Lambda = 0.09\,\text{Å}^{-1}$ [14]. The best available measure for existence of this state is the pair-correlation function. It is expected not to converge towards 1, or any stable value, like a standard RDF would. Results shown in Fig. 5.2a confirm this notion - at this density, system is not a liquid confined to the center of the pore, so the LL model is not valid.
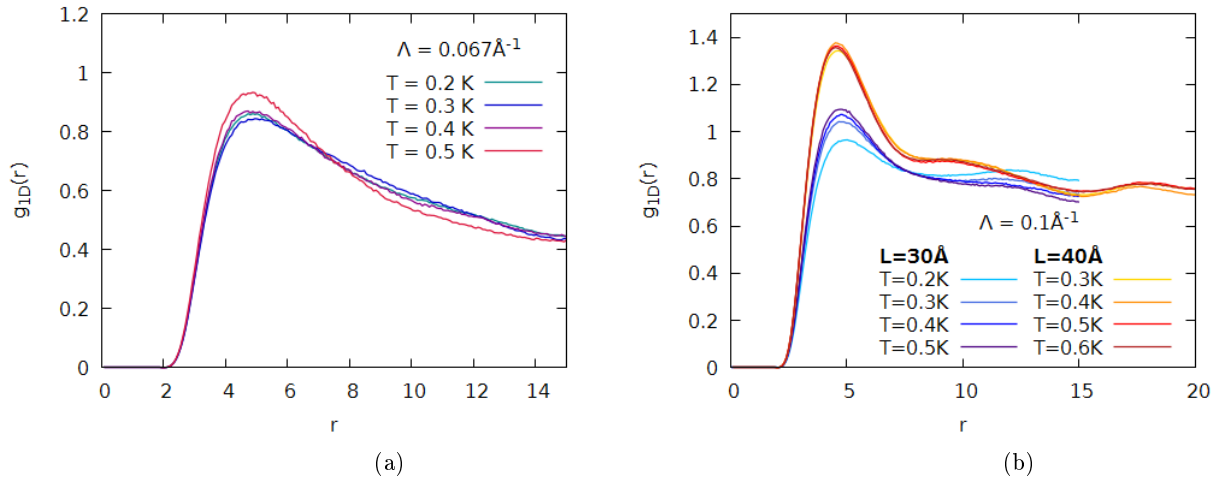

(a) (b)

Figure 5.2: (a) Pair-correlation function $g_{1D}(r)$ for density of $\Lambda = 0.067\,\text{Å}^{-1}$, with pore length $L = 15\,\text{Å}$ at various temperatures. These functions deviate from a standard RDF profile of a liquid system and match a system below spinodal point. (b) Pair-correlation function $g_{1D}(r)$ of density of $\Lambda = 0.1\,\text{Å}^{-1}$ for various pore lengths and temperatures. These results show a more common RDF profile, but still non-converging and influenced by sporadic spinodal decomposition.

Similarly, at density $\Lambda = 0.1\,\text{Å}^{-1}$, the system also occasionally enters the regime of spinodal instability, although this is not equally pronounced by RDF-s shown in Fig. 5.2b. For comparison, consider density $\Lambda = 0.133\,\text{Å}^{-1}$ that we already discussed in Fig. 4.6a. Even though these RDF-s also don't converge to 1, they still reach stability at some point. We can attribute these non-typical behaviors to finite-size effects, oscillations normally found in pair-correlation functions and the artificial reformulation of the real $g(r)$ into 1D-scaling $g_{1D}(r)$ in Eq. 4.3. Still, pair-correlation function at this density is under a great influence of finite-size effects that would likely be reduced at lengths larger than $L = 30\,\text{Å}$. Other than this, RDF-s of $\Lambda = 0.133\,\text{Å}^{-1}$ don't deviate greatly from a common profile of a liquid system.

All of these results can be compared to $\Lambda = 0.2\,\text{Å}^{-1}$ density RDF shown in Fig. 5.3. This function exhibits all the expected characteristics - oscillations pronounced at higher density, visible convergence to 1, and less susceptibility to finite-size effects than RDF-s of lower pore length presented so far. Liquids at higher densities display solid-like features [14], as indicated by oscillations in these RDF-s.
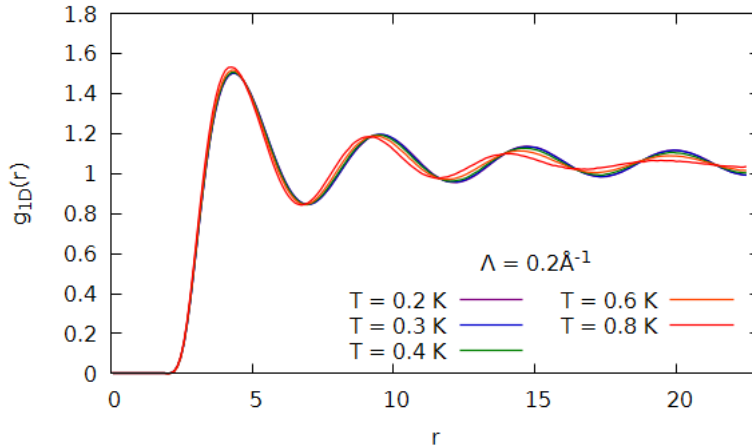

Figure 5.3: Pair-correlation function $g_{1D}(r)$ for density of $\Lambda = 0.2\,\text{Å}^{-1}$, with pore length $L = 45\,\text{Å}$ at various temperatures. The functions show oscillations expected from this density and convergence to 1 - regular behavior for an RDF of system like this.

Still, besides spinodal density, the question remains why the results are so incompatible with the LL predictions. Possibility of a crossover to Bose glass has been considered. In this process, a system in disorder falls into a localized phase [4]. In other words, domains are formed, consisting of "lakes" of condensate separated by the repulsive regions of disordered potential [6]. If the external potential is periodic instead of disordered, one could consider a crossover into a Mott insulator [27], with the main difference being that Bose glass is a compressible phase, unlike incompressible Mott insulator. Both of these phases are characterized by absence of superfluidity, with superfluid density being zero. Specifically, Bose glass is locally still in superfluid phase, but macroscopic superfluid

density is negligible. Both crossovers are also marked by a discontinuity in the value of Luttinger parameter K found in Eq. 2.45. However, we have not detected any sudden drop in superfluid density or a discontinuity in Luttinger parameter that could signal a transition into Bose glass. Hence, the possibility of this crossover has been discarded. In fact, we have not detected, for any available physical quantity, a sudden drop or rise that might signal any kind of crossover.

The Luttinger parameter is defined in LL theory as $K = \hbar\pi\sqrt{\kappa\rho^3/m}$, where κ is the compressibility. Preliminary studies show that the disorder has no significant influence on the values of K. In 1D, it is expected that superfluidity is robust to disorder for $K > 3/2$, while this does not hold for lower K [14]. These predictions were not observed in our data - the fits are bad for all used densities. The region of $K > 3/2$ with no spinodal decomposition is very small, practically only at $\Lambda = 0.133\,\text{\AA}^{-1}$. These results are influenced by finite-size effects that reduce the accuracy of calculated K, and more low-density calculations are needed for improvement. Furthermore, for $\Lambda = 0.2\,\text{\AA}^{-1}$ and $\Lambda = 0.25\,\text{\AA}^{-1}$, the parameter is certainly $K < 3/2$ and a sudden drop in superfluid density is expected. This was also not observed - we only detected high values of χ^2. A possible explanation is once again quasi-1D nature of our system, as discussed before. This should be explored by further calculations.

So far, the only working theory for this system is the Tomonaga-Luttinger liquid model, and it fails to explain the results. Other than that, there is no good theoretical explanation. At this point, further study is required, as always. But, we are still restricted by computational limitations and lacks of resources to gather additional data that would confirm or further disprove the LL model. Currently, the only certain results is disagreement with the LL model, so any other judgment has to be put on hold for now.

5.1 Conclusion

To sum up, we have conducted a numerical study by a series of PIMC simulations of bosonic helium in nanopores of $R = 3\,\text{\AA}$ with atoms of impurities scattered around the surface at one atom per unit of length on average. Underlying theory of path integral quantum mechanics and the anticipated Tomonaga-Luttinger scaling model was provided as well. This 1D liquid in disorder, confined to the center of the pore, was expected to scale as a Luttinger liquid, as confirmed by a previous study [3] for narrow nanopores without disorder. This was not the case; all of the data we acquired fits badly with predictions of the theoretical model. LL parameters are lower in value than the uniform calculations that match the theoretical predictions, and χ^2 values are large, for every used linear density of ^{4}He. All of this indicates that the addition of disorder breaks the LL scaling.

Unfortunately, computational limitations an a lack of alternative theoretical models prevent us from making any sound conclusions for now. The study doesn't stop there, though. Current results [14] are in submission and further calculations are in progress, particularly with larger pore lengths L to reduce the finite-size effects and enable a more accurate description of physical regimes determined by the value of Luttinger parameter

K. As a future prospect, possible expansion of this study could include a better classification of disorder by introducing a measuring quantity, or a more thorough examinations of duplicating the disorder and thus making it periodic in length. Averaging the results over various models of disorder would provide a more conclusive and realistic picture of the effects of disorder on low energy liquid systems in narrow nanopores. Alternatively, a better theoretical model could be constructed, which was already initiated by introduction of dynamical superfluid fraction.

All the results showcased by this study indicate that 1D systems in disorder are still certainly a matter of discussion and require additional measurements, calculations and derivations. With this outlook for future, we conclude the presented preliminary research of low energy one-dimensional disordered helium.

Bibliography

[1] D. M. Ceperley: Path Integrals in the Theory of Condensed Helium, Rev. Mod. Phys. **67**, 2 (1995)

[2] R. P. Feynman: Space-Time Approach to Non-Relativistic Quantum Mechanics, Rev. Mod. Phys. **20**, 2 (1948)

[3] L. Vranješ Markić, H. R. Glyde: Superfluidity, BEC and the Dimensions of Liquid ^{4}He in Nanopores, Phys. Rev. B **92**, 064510 (2015)

[4] M. A. Cazalilla, R. Citro, T. Giamarchi, E. Orignac, M. Rigol: One Dimensional Bosons: From Condensed Matter Systems to Ultracold Gases, Rev. Mod. Phys. **83**, 1405 (2011)

[5] R. Rota: Path Integral Monte Carlo and Bose-Einstein Condensation in Quantum Fluids and Solids, Ph.D. thesis (2011)

[6] B. Svistunov, E. Babaev, N. Prokof'ev: Superfluid States of Matter, CRC Press (2015)

[7] T. H. Hanson: Fermi and Luttinger Liquids, lecture notes for the course *Quantum Field Theory for Condensed Matter*, Stockholm University

[8] T. Giamarchi: Quantum Physics in One Dimension, Clarendon Press, Oxford (2003)

[9] N. T. Brönn: Luttinger Liquids, essay, University of Illinois (2007)

[10] F. D. M. Haldane: Effective Harmonic-Fluid Approach to Low-Energy Properties of One-Dimensional Quantum Fluids, Phys. Rev. Lett. **47**, 1840 (1981)

[11] H. J. Schulz, G. Cuniberti, P. Pieri: Fermi Liquids and Luttinger Liquids, arXiv:cond-mat/9807366v2 [cond-mat.str-el] (1998)

[12] E. L. Pollock, D. M. Ceperley: Path-Integral Computation of Superfluid Densities, Phys. Rev. B, **36**, 16 (1987)

[13] A. Del Maestro, I. Affleck: Interacting Bosons in One Dimension and the Applicability of Luttinger-Liquid theory as Revealed by Path Integral Quantum Monte Carlo Calculations, Phys. Rev B **82**, 060515(R) (2010)

[14] L. Vranješ Markić, H. Vrcan, Z. Zuhrianda, H. R. Glyde: Superfluidity, BEC and the structure in 1D Luttinger Liquids, in preparation (2017)

[15] L. Vranješ Markić, P. Stipanović: Stohastičke Simulacije u Klasičnoj i Kvantnoj Fizici, internal script, University of Split (2016)

[16] H. Gould, J. Tobochnik, W. Christian: An Introduction to Computer Simulation Methods Applications to Physical Systems (2016)

[17] M. Bonisegni, N. V. Prokof'ev, B. V. Svistunov: Worm Algorithm and Diagrammatic Monte Carlo: a New Approach to Continuous-Space Path Integral Monte Carlo Simulations, Phys. Rev. E **74**, 036701 (2006)

[18] M. Bonisegni, N. V. Prokof'ev, B. V. Svistunov: Worm Algorithm for Continuous-Space Path Integral Monte Carlo Simulations, Phys. Rev. Lett. **96**, 070601 (2006)

[19] M. Boninsegni: Permutation Sampling in Path Integral Monte Carlo, J. Low Temp. Phys. **141**, 1/2 (2005)

[20] S. Jang, S. Jang, G. A. Voth: Applications of Higher Order Composite Factorization Schemes in Imaginary Time Path Integral Simulations, J. Chem. Phys. **115**, 7831 (2001)

[21] S. A. Chin: Symplectic Integrators from Composite Operator Factorizations, Phys. Lett. A **226**, 344-348 (1997)

[22] V.I. Yukalov: Basics of Bose-Einstein Condensation, arXiv:1105.4992v1 [cond-mat.stat-mech] (2011)

[23] B. Kulchytskyy, G. Gervais, A. Del Maestro: Local Superfluidity at The Nanoscale, Phys. Rev. B **88**, 064512 (2013)

[24] R. A. Aziz, F. R. W. McCourt, C. C. K. Wong: A New Determination of the Ground State Interatomic Potential for He_2, Mol. Phys. **61**, 1487 (1987)

[25] N. V. Prokof'ev, B. V. Svistunov: Two definitions of superfluid density, Phys. Rev. B **61**, 11282 (2000)

[26] J. W. Cahn: Phase Separation by Spinodal Decomposition in Isotropic Systems, J. Chem. Phys. **42**, 93 (1965)

[27] G. Boéris, L. Gori, M. D. Hoogerland, A. Kumar, E. Lucioni, L. Tanzi, M. Inguscio, T. Giamarchi, C. D'Errico, G. Carleo, G. Modugno, L. Sanchez-Palencia: Mott transition for strongly interacting one-dimensional bosons in a shallow periodic potential, Phys. Rev. A **93**, 011601(R) (2016)